RASTI 000, 1–19 (2025) Preprint 13 October 2025 Compiled using rasti LaTeX style file v3.0

An X-ray scattering technique for characterising Mercury's carbon enrichments with BepiColombo

Adam R. D. Fox,[1]⋆ Adrian Martindale,[1] Tiffany L. Barry,[2] Simon T. Lindsay,[1] Bernard Charlier,[3] Olivier Namur,[4] Graeme P. Hall,[1] Emma J. Bunce,[1] John C. Bridges,[1] Julia A. Cartwright,[1] and Tuomo Tikkanen[1]
[1] *Space Park Leicester, School of Physics and Astronomy, University of Leicester, Leicester, LE4 5SP,UK*
[2] *School of Geography, Geology and the Environment, University of Leicester, Leicester, LE1 7RH,UK*
[3] *Department of Geology, University of Liège, 4000 Sart-Tilman, Liège, Belgium*
[4] *Department of Earth and Environmental Sciences, KU Leuven, 3001, Leuven, Belgium*

Accepted XXX. Received YYY; in original form ZZZ

ABSTRACT

Spatially resolved observations of carbon on Mercury's surface are of great scientific importance for the origin and speciation of volatile elements and for the reflectance properties of the surface, notably for Mercury's Low Reflectance Material (LRM). However, such measurements are extremely challenging, even with BepiColombo's state-of-the-art instrument suite. To overcome the issues with direct measurement, we have created an entirely new indirect method for characterising localized carbon enrichments on Mercury with the Mercury Imaging X-ray Spectrometer (MIXS). Elevated abundances of low atomic number elements increase the spectral intensity of scattered X-rays. This provides a proxy for graphite enrichment which is the currently preferred hypothesis for the dominant darkening phase in the LRM. We report experimental X-ray measurements including scattered X-rays and XRF for a library of reference materials and graphite-spiked samples of varying abundances using the MIXS Ground Reference Facility. By modelling the results using established theory and databases of X-ray fundamental parameters, we validate the method and enable reliable extrapolation to future MIXS observations. Using modelled solar flares, fitted to solar X-ray observations from the MESSENGER mission, we estimate that integration times of hundreds of seconds during intense flares can resolve increases in scatter intensity created by various expected carbon abundances. Through detailed analysis we find that it may be possible to place an upper bound on graphite content, strengthening the scientific rationale for dedicated 'stare' observations of LRM rich regions during BepiColombo's extended mission.

Key words: MIXS – BepiColombo – Low Reflectance Material – X-ray Scatter – Carbon – Data Methods

1 INTRODUCTION

The Mercury Imaging X-ray Spectrometer (MIXS) (Bunce et al. 2020) is onboard the Mercury Planetary Orbiter (MPO), one of two spacecraft which comprise ESA/JAXA's BepiColombo mission (Benkhoff et al. 2021) which will commence science operations from Mercury orbit in 2027. MIXS will probe the elemental composition of the upper tens of microns of Mercury's surface. The fluorescent signal of characteristic X-rays released from surface atoms which have been excited by solar coronal X-rays will be interpreted to produce elemental abundance maps of the planet's surface. MIXS data will build on the elemental maps produced following NASA's MESSENGER mission (Solomon et al. 2018; Nittler et al. 2020, 2023) from the X-ray Spectrometer, XRS (Schlemm et al. 2007), onboard. MIXS comprises two instrument channels: the collimating MIXS-C, which will collect large fluxes continuously, and MIXS-T, an imaging telescope which will provide high spatial resolution data during periods of enhanced solar activity.

MESSENGER left several unresolved questions that it is hoped BepiColombo will provide the data to answer. One key question surrounds the origin of Mercury's Low Reflectance Material (LRM). LRM was identified as a major spectral unit after the first MESSENGER flyby (Robinson et al. 2008; Blewett et al. 2009) from imagery by the Mercury Dual Imaging System (MDIS) (Hawkins et al. 2007). The defining spectral features of LRM include its low albedo, up to 30% darker than the global average (Robinson et al. 2008; Denevi et al. 2009) and a comparatively blue sloped and smooth reflectance spectrum in visible and near infrared, which can include a broad depression centred near 600 nm (Robinson et al. 2008; Denevi et al. 2009; Murchie et al. 2015).

The interpretation of these features has been that a 'darkening agent' is present globally and enriched in the LRM, reducing its albedo to the levels observed (Robinson et al. 2008; Denevi & Robinson 2008; Riner et al. 2009; Denevi et al. 2009). Several darkening agents have been considered, since it was determined that nanophase Fe alone, as a product of space weathering, was insufficient to produce the spectral properties of the LRM (Blewett et al. 2009; Murchie et al. 2015). Initial candidate darkening agents, by lunar analogy, included ilmenite and ulvospinel which, subsequently, were also excluded due

---

⋆ E-mail: ardf1@le.ac.uk

to incompatibility with measured, low Fe and Ti abundances (Nittler et al. 2011; Evans et al. 2012; Weider et al. 2014; Cartier et al. 2020).

Higher than expected sulphur abundances (~1-4 wt%) led to suggestions of sulphides contributing to the darkening of Mercury's surface, with spectra from MDIS and the Mercury Atmospheric and Surface Composition Spectrometer (MASCS) (McClintock & Lankton 2007) only sensitive to extremely high (>~70 wt%) abundances of CaS and MgS (Izenberg et al. 2014; Murchie et al. 2015). Murchie et al. (2015) considered several proposed darkening agents including Ca, Mg and Fe sulphides, ilmenite, carbon and nanophase/metallic Fe. Of the sulphides tested by those authors, all were brighter than Mercury's Northern Volcanic Plains which they consider as precursor material with assumed minimal darkening agent, on the basis of being the opposing spectral end member to LRM. The presence of sulphides is not forbidden by these results and sulphides may play an important role as a volatile component in hollows formation (Blewett et al. 2011, 2013, 2016; Thomas et al. 2014; Barraud et al. 2020, 2023), however higher levels of thermal darkening are required than have currently been observed, if sulphides are the dominant darkening phase for the LRM (Thomas et al. 2016; Murchie et al. 2015). Ilmenite was shown, even with elemental abundance constraints, to be capable of matching the reflectance of the Northern hemisphere, however, not realistically the LRM (Murchie et al. 2015).

The remaining plausible darkening agent is carbon which has been considered in the form of graphite (Murchie et al. 2015; Vander Kaaden & McCubbin 2015; Peplowski et al. 2015, 2016; Klima et al. 2018). Carbon had initially been considered by Denevi et al. (2009), however other phases were believed to be more probable. Spectral modelling by Murchie et al. (2015) showed that by considering Northern Volcanic Plains material and graphite in their anticipated grain sizes, <1 wt% graphite was required to match average spectra of the Northern hemisphere and ~5 wt% could replicate the LRM. The authors also acknowledge that although nanophase Fe cannot replicate the LRM alone, a combination with coarser grained microphase Fe remained plausible. Subsequent work has suggested that smaller abundances of graphite could achieve the same effect (Xu et al. 2024). Spectral modelling has been extended to explore the darkening effect of some additional forms of carbon, e.g. sub-microscopic amorphous carbon (Trang et al. 2017), whilst other forms such as carbides remain to be explicitly evaluated.

The spatial distribution of LRM shows a strong association with crater ejecta, as well as within large expanses of heavily cratered regions with overlapping ejecta (Robinson et al. 2008; Denevi et al. 2009; Klima et al. 2018). These observations suggest that LRM is excavated from depth during impacts (Denevi & Robinson 2008; Rivera-Valentin & Barr 2014; Murchie et al. 2015; Klima et al. 2018). This supports the presence of a subsurface layer of LRM, endogenic in origin and exhumed to the surface. Such emplacement is in agreement with work by Vander Kaaden & McCubbin (2015) in which the authors propose the presence of a primary graphite flotation crust which has been buried by subsequent volcanism. Their proposal being based on having identified that in an early Mercurian magma ocean, graphite would be the stable phase of carbon within the mantle and would be the only buoyant mineral. Other proposed endogenic sources may also be consistent with a graphite-rich primary crust (Lark et al. 2023) or with emplacement of LRM material in the secondary crust via volcanism (Xu et al. 2024). Exogenic delivery from cometary impactors have also been considered (Bruck Syal et al. 2015), but is in weaker agreement with the expressed distribution of LRM (Klima et al. 2018).

MESSENGER made observations which provided further support for graphite/carbon as the darkening agent in the LRM. Firstly, a Northern hemisphere average carbon abundance of 1.4±0.9 wt% (1σ) was estimated by the Gamma-Ray Spectrometer (Peplowski et al. 2015; Goldsten et al. 2007). The measurement has large uncertainties due to the need to deconvolve the signal from the spacecraft's own carbon structure and stronger planetary oxygen signal. For this reason, a definitive detection of carbon cannot be confirmed. However, a significant body of supporting evidence has been formed, including measurements of increased thermal neutron flux over three regions of LRM (Peplowski et al. 2016) during MESSENGER's low altitude campaign. The neutron measurements are consistent with local carbon enrichments of 1.1 to 3.1 wt% in the regions analysed (Peplowski et al. 2016). This enhancement is in agreement with the source being carbon, in opposition to other proposed darkening agents such as those containing Fe, which has a much larger neutron-absorption cross-section. Additionally, recent work to re-evaluate Mariner-10 vidicon data by Sonke & Robinson (2024) finds further supporting evidence for carbon's presence with an increased reflectance at wavelengths shorter than the MDIS range. Modelling of spectra from the Visible and Infrared Spectrograph (VIRS) component of the MASCS instrument by Trang et al. (2017) found a best-fitting global average abundance for submicroscopic amorphous carbon of 1.9 wt% in conjunction with 3.5 wt% submicroscopic Fe (inconsistent with XRS estimates; Weider et al. (2014)). The results of Trang et al. (2017) do not show a definitive correlation with the LRM for either amorphous C or Fe. However, their modelling did not account for the additional presence of graphitic carbon which would darken the 'host' material.

MIXS will directly evaluate the hypotheses of several proposed darkening agents with spatially-resolved fluorescence observations of Low Reflectance Material. Sulphur abundances will be evaluated over large spatial scales by MIXS-C during normal operation as sulphur fluorescence requires only moderate solar activity; further spatially-resolved sulphur measurements will also be possible during periods of enhanced solar activity with MIXS-T. During solar flares, MIXS will provide the opportunity to observe Fe enhancements through K-series emission (6404 eV), doing so with a more homogeneous distribution of footprints than was the case for MESSENGER. Whilst there will be coverage gaps, ongoing work will investigate the possibility of observing Fe during quiescent periods through the L-line (705 eV). However, deriving quantitative information from the L-line will be challenging due to limited knowledge of the solar spectrum at low energies. The leading candidate darkening agent, graphite, will not be directly or exclusively sensed by MIXS, or necessarily by any of the instruments onboard BepiColombo (such as those discussed below). There is thus a large motivation to provide further evidence either in support of, or against, carbon as the darkening agent in the LRM and any mapping of carbon abundance or its abundance limit across the surface (see e.g. Rothery et al. (2020)).

BepiColombo provides an opportunity to probe deeper into the LRM's properties through its instrument suite, and the orbit of MPO offers the chance to observe LRM located in the Southern hemisphere with much more detail than ever before. In addition to MIXS, BepiColombo's instrument suite notably includes the Mercury Radiometer and Thermal Infrared Spectrometer (MERTIS) (Hiesinger et al. 2020) and the Visible and near-Infrared Hyperspectral Imager (VIHI) channel of the Spectrometer and Imagers for MPO Bepicolombo Integrated Observatory SYStem (SIMBIO-SYS) (Cremonese et al. 2020). In this work, we present an indirect, X-ray scattering-based method which may provide the only spatially resolved geochemical evidence for carbon enrichments in Mercury's LRM. We verify this method with laboratory measurements and predict the sensitivity of the observations MIXS will make from Mercury orbit.

2 METHODS

2.1 Rationale

Geochemical sensing and mapping of carbon on Mercury's surface is of great scientific value in the context of the LRM, however abundance estimates will not be recoverable from the fluorescent carbon signal, due to a number of factors:

(i) Most importantly, the carbon fluorescent signal itself is expected to be inherently weak. Carbon has a very low interaction cross-section with soft X-rays, making it largely transparent, with most interactions occurring in the surrounding matter. It also has a low fluorescence yield, meaning few of the photoelectric absorptions that do take place result in the emission of a characteristic X-ray photon.

(ii) Carbon K emission is produced at just 277 eV, with the absorption edge at 284 eV. These energies fall well below the practical threshold of SIXS-X, MPO's solar X-ray monitor, at ∼1 keV (Huovelin et al. 2020) and in a region where the solar X-ray spectrum is highly temporally variable. This low energy absorption edge also means carbon is more likely than other elements to be triggered as secondary fluorescence. For these reasons, the exciting flux is poorly characterized and determining abundance estimates is unlikely with MIXS.

(iii) During nominal operations, MIXS-T will incorporate a data telemetry threshold above the oxygen-K line at 525 eV (Bunce et al. 2020) due to bandwidth constraints.

(iv) Carbon-K emission is below the specified lower energy limit of MIXS and although detector performance has exceeded this and is currently calibrated at the carbon fluorescence energy (Majewski et al. 2014), radiation damage during the mission may raise the lower energy threshold above this (Bunce et al. 2020). At this energy, the detector quantum efficiency is also low and significant attenuation is produced by MIXS' optical filters.

Thus, an alternative method of sensing carbon enrichment is required. Despite the challenges in observing a fluorescent signal from carbon, its presence may be detected in another way, described in the following section.

2.2 An alternative approach to measuring carbon

The background observed within a spectrum from a remote-sensing planetary XRF instrument is partially attributable to re-distributed fluorescence counts, electronic noise and galactic cosmic rays. The dominant sources however, are solar X-rays which have been scattered from the planetary surface towards the instrument, as well as particle-induced background which is greatly enhanced during discrete events (Fraser et al. 2010).

For incident soft X-rays at higher energy than all major absorption edges in a sample, low atomic number (Z) elements (i.e. Z<10) contribute more intense scatter than the major rock forming elements. Scattered X-rays have previously been used to determine the average atomic number of targets excited by line emission sources and thus make inferences about the presence of low-Z elements (Campbell et al. 2013; Hodoroaba & Rackwitz 2014; Perrett et al. 2016). Such methods use the ratio of inelastic to elastic scatter peaks, however such a technique is incompatible with the polychromatic and temporally-variable X-ray source that is the solar corona. Figure 1a shows the modelled intensity of X-rays scattered from elements between Z=4 and Z=26. Both X-rays produced by elastic and by inelastic scattering are modelled, where the final, scattered energy is 8.5 keV . A rapid increase in scattered X-ray intensity is shown with decreasing atomic number. Scatter intensities from mixtures are not linearly correlated with abundance however, as low-Z materials have smaller interaction cross-sections than heavier elements.

The scattering properties displayed in Figure 1a allow us to propose a new method for gathering supporting evidence of carbon enrichment in LRM (or lack thereof). If carbon is the dominant darkening agent in the LRM, we hypothesise that X-ray observations over dense patches of LRM will measure increased intensities of scattered X-ray background in comparison with surrounding material of similar bulk composition. Alternatively, if the darkening agent is a heavier phase such as nanophase and/or microphase iron, the intensity of scattered X-rays from LRM will either show no difference to, or a reduction from, levels in surrounding material (see Supplementary Figure 1 for modelled effects of different darkening phases).

2.3 Modelling the scattered X-ray intensity

With knowledge of target bulk composition, illuminating spectrum and some of the fundamental parameters for the interaction of X-rays with matter, the intensity of scattered X-rays can be predicted. We start from the Beer-Lambert law for linear attenuation of light:

$$I_{\gamma}^{T} = I_{\gamma}^{0} e^{-\mu_{\gamma}^{\tau} \rho x} \tag{1}$$

where I_{γ}^{T} and I_{γ}^{0} represent the transmitted and incident intensity at energy γ through a distance x in a material of density ρ with a total mass attention coefficient at energy γ of μ_{γ}^{τ}. All terms are defined within Table 1. The mass attenuation coefficient is calculated as the sum of the mass-fraction weighted coefficients of each constituent chemical element, i.e.

$$\mu_{\gamma}^{\tau} = \sum_{\zeta} W_{\zeta} \mu_{\gamma\zeta}^{\tau} \tag{2}$$

where W_{ζ} is the weight-fraction of the target material that is element ζ.

To consider X-ray interactions taking place in an infinitesimal window of path length dx at penetration distance x, first we differentiate Equation 1 to find the change in transmitted intensity over this path.

$$\frac{\delta I_{\gamma}^{T}}{dx} = -\mu_{\gamma\zeta}^{\tau} \rho I_{\gamma}^{0} e^{-\mu_{\gamma\zeta}^{\tau} \rho x} \tag{3}$$

The modulus of this being R_A, the interaction rate in the region dx, in dimensions of events per unit time.

$$R_A = \mu_{\gamma\zeta}^{\tau} \rho I_{\gamma}^{0} e^{-\mu_{\gamma\zeta}^{\tau} \rho x} dx \tag{4}$$

The contribution from each interaction mechanism can be considered separately, the total mass attenuation coefficient is made up of photoelectric absorption, Rayleigh (μ^R) and Compton (μ^C) scattering and, at much higher energies than are considered here, pair and triplet production. Equation 4 can thus be represented through its Rayleigh and Compton parts:

$$R_A^R = \mu_{\gamma}^{R} \rho I_{\gamma}^{0} e^{-\mu_{\gamma}^{\tau} \rho x} dx \tag{5}$$

$$R_A^C = \mu_{\gamma'}^{C} \rho I_{\gamma'}^{0} e^{-\mu_{\gamma'}^{\tau} \rho x} dx \tag{6}$$

where γ' refers to the higher incident energy that produces a Compton scattered photon with energy γ, this energy shift is consistent for scattering from any element through a given angle.

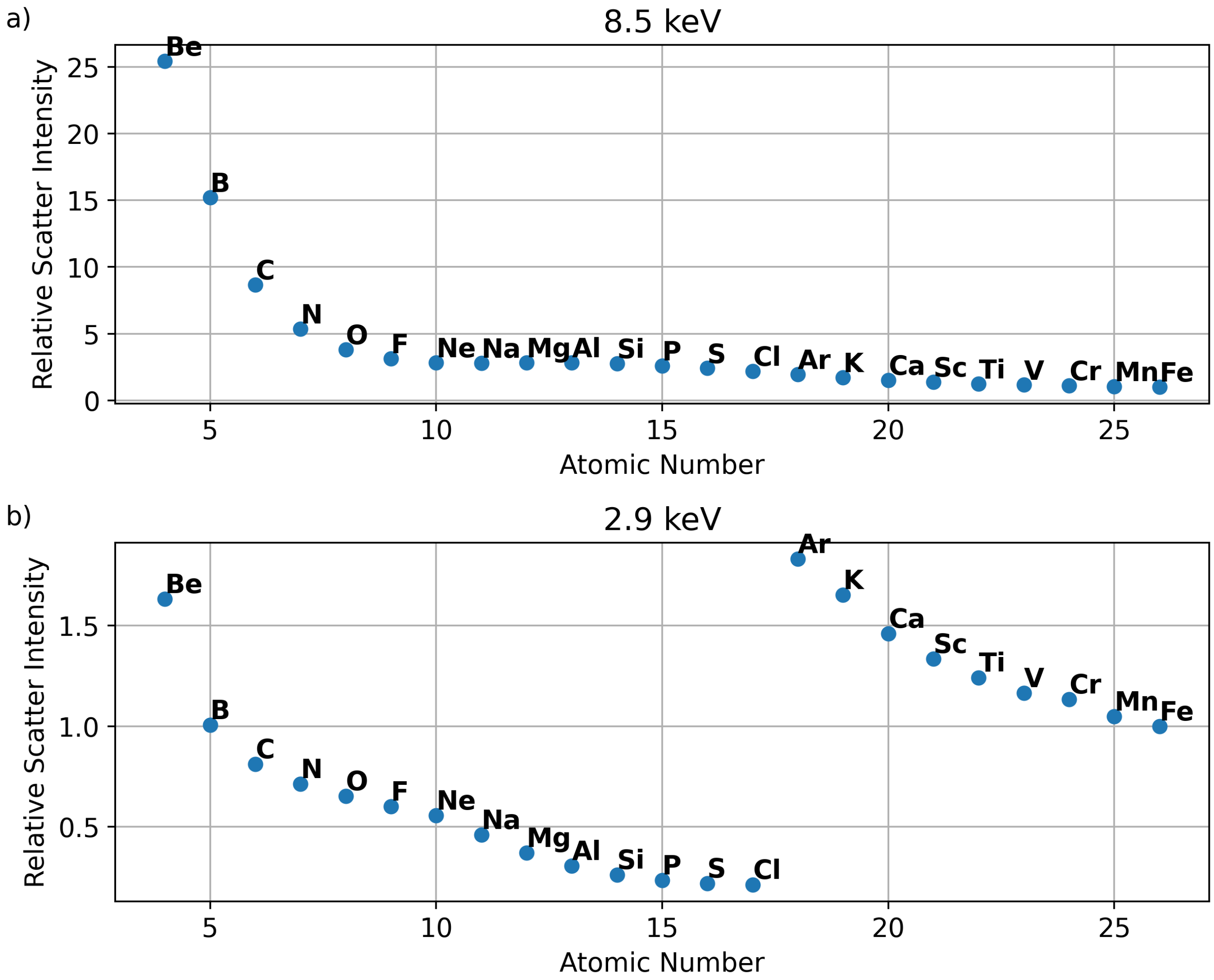

Figure 1. Relative scatter intensities (ratioed to Fe) modelled with Equation 10 for element targets observed at 8.5 (a) and 2.9 keV (b). Incidence angle (θ) = 30°, emergence angle (ϕ) = 0°.

Next, an additional Beer-Lambert term is added to account for the attenuation of the outgoing X-ray through the target to the detector; this path length is calculable as: $\frac{xcos(\theta)}{cos(\phi)}$. Where θ is the incidence angle and ϕ is the emergence angle, both measured relative to the surface normal.

Thus, for a scatter angle φ:

$$I^R_{\gamma\varphi} = \mu^R_\gamma \rho I^0_\gamma e^{-\mu^\tau_\gamma \rho x} e^{-\mu^\tau_\gamma \rho \frac{xcos(\theta)}{cos(\phi)}} \tag{7}$$

$$I^C_{\gamma\varphi} = \mu^C_{\gamma\prime} \rho I^0_{\gamma\prime} e^{-\mu^\tau_{\gamma\prime} \rho x} e^{-\mu^\tau_\gamma \rho \frac{xcos(\theta)}{cos(\phi)}} \tag{8}$$

Lastly, this must be integrated across all energies in a range of interest and across all path lengths from the target surface to an extinction path length, P_{max}. The total scatter intensity, I^S, is the sum of both interactions, multiplied by the detector solid angle, $\delta\Omega$:

$$I^S = \rho \int_{E_{min}}^{E_{max}} \int_0^{P_{max}} I^0_\gamma \mu^R_\gamma e^{-\mu^\tau_\gamma \rho x\left[1+\frac{cos(\theta)}{cos(\phi)}\right]} + I^0_{\gamma\prime} \mu^C_{\gamma\prime} e^{-\rho x\left[\mu^\tau_{\gamma\prime}+\mu^\tau_\gamma \frac{cos(\theta)}{cos(\phi)}\right]} dxdE \times \delta\Omega \tag{9}$$

When these path length integrals are evaluated for $P_{max} = \infty$, i.e. an infinitely thick sample approximation which is valid both at Mercury and for the samples analysed in Section 3, the result is as follows:

$$I^S = \int_{E_{min}}^{E_{max}} \frac{I^0_\gamma \mu^R_\gamma}{\mu^\tau_\gamma\left[1+\frac{cos(\theta)}{cos(\phi)}\right]} + \frac{I^0_{\gamma\prime} \mu^C_{\gamma\prime}}{\left[\mu^\tau_{\gamma\prime}+\mu^\tau_\gamma \frac{cos(\theta)}{cos(\phi)}\right]} dE \times \delta\Omega \tag{10}$$

Equation 10 is evaluated throughout this paper, firstly, to predict measurements made in laboratory experiments (Section 3) to verify this methodology. Subsequently, observations at Mercury are predicted to evaluate the effectiveness of this technique at detecting the spectral effects of carbon enrichment in the LRM (Section 4).

The predictions require Equation 10 to be evaluated numerically in

Table 1. Definition of symbols used in the equations for predicting X-ray scatter intensity. Square brackets denote typical units.

Symbol	Definition
x	Length dimension along X-ray path [cm]
γ	A specific energy range
ζ	A specific element
ρ	The density of the target material [g cm^{-3}]
W_ζ	Weight fraction of element ζ
I_γ^T	Transmitted X-ray intensity in energy range γ [photons s^{-1}]
I_γ^0	Incident X-ray intensity in energy range γ [photons s^{-1}]
$I_{\gamma\varphi}^R$	Rayleigh scattered X-ray intensity in energy range γ and at scatter angle φ [photons s^{-1} sr^{-1}]
$I_{\gamma\varphi}^C$	Compton scattered X-ray intensity received in energy range γ and at scatter angle φ [photons s^{-1} sr^{-1}]
$I_{\gamma\varphi}^S$	Total scattered X-ray intensity received in energy range γ and at scatter angle φ [photons s^{-1} sr^{-1}]
$\mu_{\gamma\zeta}^\tau$	Total mass attenuation coefficient of element ζ in energy range γ [cm^2 g^{-1}]
$\mu_{\gamma\zeta\varphi}^R$	Differential Rayleigh mass attenuation coefficient of element ζ, scattered through angle φ at energy γ [cm^2 g^{-1} sr^{-1}]
$\mu_{\gamma\zeta\varphi}^C$	Differential Compton mass attenuation coefficient of element ζ, scattered through angle φ at energy γ [cm^2 g^{-1} sr^{-1}]
θ	Incidence angle (relative to surface normal)
ϕ	Emergence angle (relative to surface normal)
φ	Scatter angle (measured from direction of travel)
dE	An infinitesimal interval of energy
dx	An infinitesimal unit of path length
$\delta\Omega$	The solid angle scattered into [sr]

discretized energy bins. This is performed with the use of attenuation coefficients from the Xraylib library (Schoonjans et al. 2011) through the Python interface. Xraylib interpolates between measured data points to provide values for any element at any desired energy and scattering angle. The Rayleigh and Compton attenuation coefficients are taken from Elam et al. (2002), with the total attenuation coefficient also including photo-ionisation data from Kissel (2000).

2.4 Developing a diagnostic technique

An appropriate method for quantifying the X-ray scatter intensity is required if we are to utilise scattering interactions to provide information about the nature of Mercury's LRM. Our method is consistent and applied throughout this paper to both our laboratory experiments and predictions of spacecraft measurements. Our chosen method involves summing the intensity of X-rays from a particular energy range of the spectrum, which is chosen such that it represents a spectral region, free of significant line emission and dominated by scattered X-rays.

The MIXS detectors have a characteristic response to X-ray photons, approximated by the energy redistribution function shown in Figure 2. This function, described more completely by Lauf (2011), shows two non-main-peak features; a Si escape peak at 1740 eV below the main peak, and a low energy tail and shelf. The accumulation of these low energy tails and shelves can, at some energies, dominate the background over scattered X-rays, thus the window we select must be higher than the highest energy peaks observed in the spectrum in order to avoid contamination from redistributed counts. The highest energy peaks anticipated to be resolved above the background are the Fe K lines, with K$_\beta$ at 7.058 keV resolved to a full-width at half-maximum of ~135 eV (Majewski et al. 2014) at the start of the mission. Nickel and Cu peaks at higher energy were not observed in all-but one of the silicate reference materials tested in Section 3; neither are these peaks referenced in analysis of MESSENGER's XRS results (Nittler et al. 2020, 2023). The sole analysed sample in which the Ni K peaks were detected has a reported Ni content of >2000 ppm.

Furthermore, for incident photons with energies below the photoelectric absorption edge of an element, their scattering contribution is much greater than for those with energies above. As a result, the dominance of low-Z material in scatter intensity is only as greatly exaggerated as in Figure 1a when the incident energy is higher than the K absorption edge of all major elements in the target. Figure 1b illustrates this, with the K-edge of elements up to Cl (Z=17) falling below the energy analysed (2.9 keV) and heavier elements having K-edges above.

Despite the constraint to consider only energies above the Fe absorption edge and fluorescence lines, analyses should also be optimized to utilise incident X-ray flux from the Sun that is greatest at lower energies. The solar spectrum exhibits a steep power law overlain by emission lines. Since scatter intensities are typically orders of magnitude lower than fluorescence line intensities from a target, maximising the incoming flux by minimising the energy range as much as can be permitted is necessary to produce statistically robust data.

We also consider whether there is a significantly optimal angular

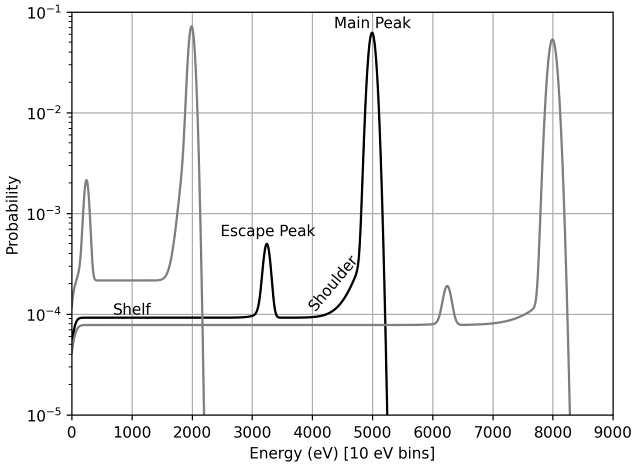

Figure 2. A model of the MIXS detector energy redistribution function displayed for 2, 5 and 8 keV photons. The features of the redistribution function are labelled and include the main peak, an escape peak for photons with energies greater than that of the Si K absorption edge and a low energy tail which extends into a shelf. For a complete description of this function see Lauf (2011).

range for scattered X-ray flux. Figure 3 includes a series of plots which assist in identifying the most suitable conditions; these plots display data sourced from the Xraylib database (Schoonjans et al. 2011).

Figures 3a and b show that the two mechanisms of scattering vary in their responses. Both increase in magnitude towards the highest scattering angles (backscatter), however Rayleigh scattering is strongest at low energies, whilst Compton is at its most intense at higher energy. It is also observable that both are a slow function of scatter angle, a property which also clear in overall scattering coefficient (Figure 3c). Thus, in the analysis for this paper, we consider standardized illumination conditions of 30° incidence angle and 0° emergence angle (this emergence angle is analogous to the nadir pointing observations MIXS will make during BepiColombo's primary mission), representing a 30° phase angle and scattering angle of 150°.

The presence of two scattering mechanisms for which detected X-rays cannot be differentiated, and which are sourced from different energies in the incidence spectrum, creates complications for combining data from multiple observations with differing solar spectral shapes. As such, it would be ideal to observe a regime in which one mechanism dominates. Despite the Figure 3c appearing to be dominated by Rayleigh scatter, the ratio of Rayleigh to Compton scattering in Figure 3d shows that, Rayleigh scattering dominates at low energies, however this drops off rapidly and by the energy of the Fe K series, ceases to be the case. Thus energy range constraints above restrict us to a range with significant contribution from both Rayleigh and Compton scattering. The challenge that this presents for combining observations is explored in Section 4.1.3.2.

After considering all the above constraints, we choose to quantify X-ray scattering by analysing the intensity of X-rays detected across the range 8.00 keV to 10.00 keV. We note that this energy window falls outside of the nominal range of telemetry for MIXS-T events. The exact upper limit is pixel dependent, owing to individual gain and offsets, however the median value is ~7 keV. Telemetry can be extended to cover this energy range, however this requires a focal plane assembly (FPA) mode cycle.

Table 2. Range of compositional abundances included in the terrestrial reference material catalogue. Compositions sourced from the GeoRem online database (Jochum et al. 2005).

	Lower Bound	Upper Bound
Oxide	wt%	wt%
Na_2O	0.03	10.59
MgO	0.01	43.51
Al_2O_3	0.15	59.20
SiO_2	34.40	97.81
P_2O_5	0.01	1.39
SO_3	0.02	0.19
K_2O	0.01	12.81
CaO	0.04	15.90
TiO_2	0.01	3.77
MnO	0.00	0.77
Fe_2O_3	0.04	55.85
Element	ppm	ppm
C	37	19 600
F	30	28 500
S	0	11 230
V	0.2	526
Cr	1.4	24 270
Co	0.2	210
Ni	1.5	2 044
Cu	1	1 230
Zn	0.6	1 300
Zr	0.7	11 000
Rb	0.3	3 600
Sr	3	4 600
Ba	1.5	4 000
Th	0.04	1 003
U	0.02	650

3 LABORATORY EXPERIMENTS

3.1 Method

3.1.1 Experiment Outline

In order to test the practicality of the theoretical method outlined in Section 2.2 and proceduralized in Section 2.4, we have carried out ground-based experiments across a range of well characterized materials. These materials are separated into two categories, the first is a collection of natural terrestrial reference materials covering a broad range of compositions described in Table 2. Secondly a series of samples were prepared synthetically, consisting of a particular reference material, '*WS-1*' (Dolerite, Whin Sill, UK), spiked with increasing graphite abundances. The composition of *WS-1* is reported in Table 3. *WS-1* is selected on basis of being a readily available and well characterized igneous rock, beyond this it does not represent a Mercury analogue. The graphite abundances within these samples range from 0 to 70 wt%, in steps of 10 wt%.

3.1.2 Sample Preparation

All samples were prepared as pressed powder pellets (example shown in Supplementary Figure 2) to ensure a homogeneous composition and smooth surface. The samples were prepared under standardized procedures which are detailed below.

The powder pellets of reference materials were prepared using 7 g of material, mixed in an agate mortar with a binder: 2.5 ml of elvacite® (20%) solubilized in acetone and stirred until complete evaporation of acetone under an infrared heat lamp. The dry powders

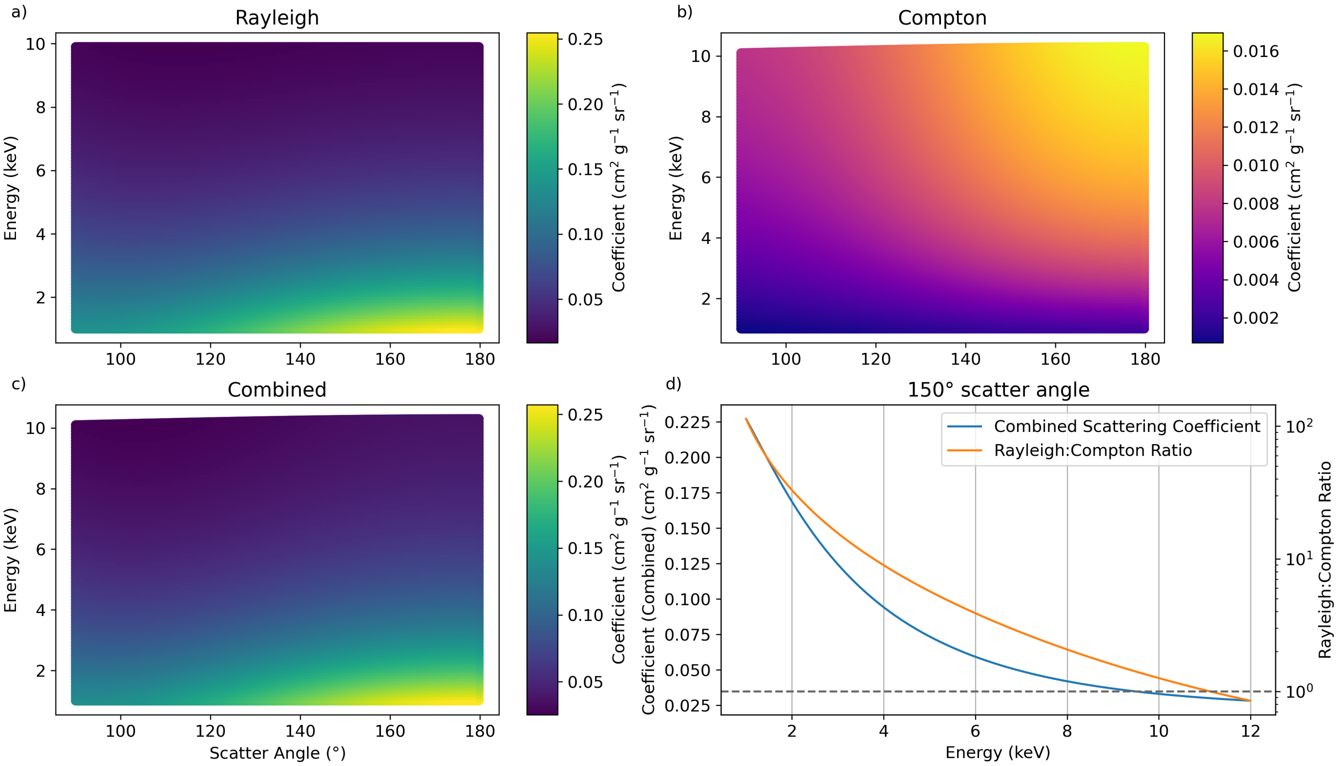

Figure 3. Scattering attenuation coefficients shown as functions of energy and scattering angle over the angular range expected during BepiColombo's primary mission. Data sourced from Xraylib (Schoonjans et al. 2011) and produced for the composition of '*WS-1*' (Table 3), a dolerite detailed in Section 3. Displayed are the Rayleigh (a), Compton (b) and Combined (Rayleigh + Compton) (c), as well as specific evaluations at a fixed scattering angle of 150° (d). Within (d) the left axis displays the Combined (Rayleigh + Compton) coefficient (blue), whilst the right axis displays the ratio of Rayleigh:Compton (orange), with the dashed horizontal line indicating a Rayleigh:Compton ratio of unity.

Table 3. Composition of WS-1 dolerite, determined by wavelength-dispersive XRF.

Element Wt %	Na_2O 2.64	MgO 5.34	Al_2O_3 13.76	SiO_2 51.40	P_2O_5 0.30	SO_3 0.19	K_2O 1.32	CaO 8.78	TiO_2 2.46	MnO 0.18	Fe_2O_3 13.48
Element ppm	V 337	Cr 49	Co 47	Ni 48	Cu 69	Zn 125	Zr 194	Rb 36	Sr 463	Ba 378	Th 3

were then pressed under 15 tons for 20 seconds, producing pellets with a diameter of 28 mm and a thickness of 3-5 mm.

For preparation of the graphite-dolerite mixtures, powders of both dolerite and graphite (*MERCK product code: 1.04206*) were dried and stirred for mixing. A binder was then added and mixed with a glass rod: Mowiol® solution is produced by dissolving beads of polyvinyl alcohol ($[CH_2CHOH]_n$) with methanol whilst being heated and then adding de-ionized water. Once thoroughly mixed, the material was pressed under 10–11 tonnes for 60 seconds. The pellets have a diameter of 32 mm and were allowed to dry for a period of >24 hours. Additional details are provided in supplementary materials.

3.1.3 *Experimental Conditions*

The samples were analysed under a standardized methodology with the MIXS Ground Reference Facility (GREF) (Bunce et al. 2020; Hall et al. 2025; Cartwright et al. 2025). The GREF is a large, high-vacuum chamber which consists of:

(i) The QM+ (qualification model) MIXS detector and electronics box,
(ii) A rotating sample stage which houses up to five samples simultaneously,
(iii) A rhodium target X-ray tube, collimated by a tungsten aperture, and
(iv) Coaxially aligned, rotating arms for the source and detector.

The rotating arms allow for replication of the full range of incidence and emergence angles MIXS will observe in orbit. As outlined in Section 2.4, the experiments described here were all carried out with an incidence angle of 30° and an emergence angle of 0°. Ray tracing of the 3D geometry shows the range and distribution of scattering angles reaching the detector under this configuration (Figure 4).

We illuminated the samples with the X-ray tube operating at an accelerating voltage of 10 kV, emission current of 0.6 mA and observed with the detector cooled to -50°C. The spectra were collected over integration times of ~3600 s and converted to intensity in units of cts s^{-1} eV^{-1} across the entire detector.

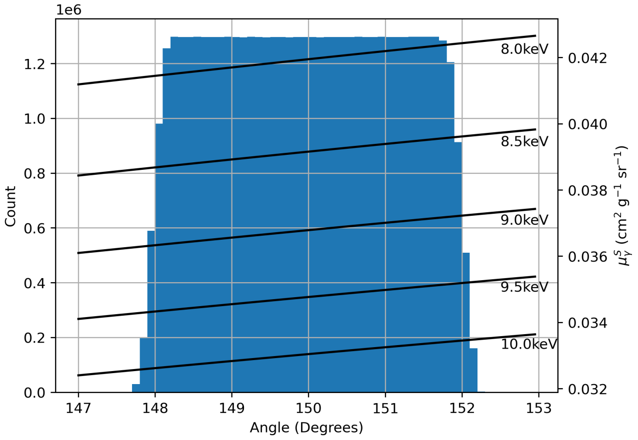

Figure 4. Blue histogram (left axis) - The distribution of scattering angles produced by the experimental configuration of GReF when centred at $\theta = 30°$, $\phi = 0°$. Black lines (right axis) - The combined scattering attenuation coefficient for energies of interest to this work over the same angular range; data from the Xraylib database (Schoonjans et al. 2011), sampled at intervals of 0.05°.

We integrated the intensity across the energy window of interest from the calibrated spectra. These results were then compared against modelled results, calculated from Equation 10 using published elemental abundances and a modelled incident spectrum. The modelling considers an energy resolution, dE, of 10 eV. The modelled incident spectrum (described fully by Hall (2022) and Hall et al. (2025)) accounts for specificities of the GREF system including attenuation by a Be window on the X-ray source and collimation.

The scatter angle we model is uniformly 150°. The lines displayed in Figure 4 show that the Xraylib coefficients used in this modelling are linear with angle across the energy range of interest at the angles produced in this experiment. Since the distribution of angles also shown in Figure 4 is approximately uniform, approximating the angle as the central value of 150° is a valid assumption.

3.2 Experimental Results

Example calibrated laboratory spectra from the reference material catalogue and from the graphite spiked samples are shown in Figures 5a and 5b, respectively. The spectra show fluorescence peaks from each of the major elements within the samples; for heavier elements, both the K_α and K_β peaks are resolvable. An additional peak feature can be seen from the Rh L-series, which is visible in the scattered flux from the X-ray source. Low-energy lines such as those from O and Na exhibit relatively small peaks as there is little illuminating flux at low energies where incident X-rays are attenuated by the Be window mentioned above. The energy window we consider for this work is highlighted in green.

Across the energy region of interest (8.00–10.00 keV), the spectra in Figure 5 show differing levels of spectral background, whilst the carbon containing samples in Figure 5b display the expected increases in scattering at higher energies with the addition of low-Z graphite. There is a turnover which exists between ∼3 and ∼5 keV, below which, the lower carbon containing samples exhibit higher spectral background. We attribute this to the reduction in the balance material (WS-1) with increasing carbon content. Lower abundances of balance elements yield smaller fluorescence peaks. The low energy shelf of the energy redistribution function (Figure 2) from these peaks therefore also reduces in magnitude with higher carbon content. This effect cannot be explained by a physical reduction in scattered X-rays as the incident flux in the very low energies is entirely attenuated by the Be windows in GREF, yet this effect persists.

The carbon fluorescence line (277 eV), overlays an increase in intensity in all spectra due to thermal noise, however we do not observe a carbon fluorescence peak which correlates with carbon content. This is an anticipated result for reasons described in Section 2.1, however, more so as there are very few incident X-rays around the absorption edge energy owing to Be windows which attenuate low energy flux from the X-ray source.

The scatter intensities integrated across the energy region of interest (8.00–10.00 keV) are displayed in Figure 6, plotted against average atomic number of each sample, $\bar{Z}$, calculated as:

$$\bar{Z} = \sum_{\zeta} W_\zeta Z_\zeta \tag{11}$$

In Figure 6, the laboratory observations and the modelled values have been normalized separately to the measurement of WS-1. This is performed due to uncertainties in the magnitude of the modelled X-ray source spectrum. This is a laboratory limitation; reconciling the modelled source spectrum and real source spectrum measurements is extremely difficult, as the count rates under direct illumination exceed the detector's maximum readout rate. Even at greatly reduced emission current, significant pileup occurs throughout the spectrum. The choice to normalize the values to the WS-1 sample in particular is arbitrary, however, with this in mind, we acquired excessively long WS-1 integration times to improve precision in its spectrum.

Figure 6 shows two main curves; the first tracks the silicate reference materials as a group, whilst the second follows the carbon-spiked samples. Both groups increase in intensity with a decrease in average atomic number, however the curvature of the reference materials is greater than the carbon-spiked samples. This change is attributed to the low X-ray interaction cross-section of carbon in comparison to the major rock forming elements. As a result, very large abundances of carbon are required for the effects of its high scattering coefficient to dominate the observed scatter. At high abundances, where carbon begins to dominate interactions, the scattering intensity rapidly increases, consistent with expectation from Figure 1.

3.3 Discussion of Experiments

The laboratory spectra shown in Figure 5 clearly demonstrate observed differences in the scattered X-ray intensity from regions of smooth continuum under the same observing conditions. Some of the samples in the catalogue were observed to exhibit evidence of X-ray diffraction. One such peak appears centred at ~9.2 keV as the graphite concentration rises, labelled α in Figure 5b. Diffraction effects are not anticipated to present themselves in the same way at Mercury as observed here due to the scales of the instruments' footprints, however effects of powder diffraction from Mercury's regolith are plausible and warrant further investigation. This particular diffraction peak only becomes resolvable in our spectra at higher carbon abundances than anticipated for Mercury, beginning to become resolved at >30 wt%.

The experimental results displayed in Figure 6, support this scatter-based method as being sensitive to changes in carbon content. The results have shown that to produce changes in scatter intensity, which are of the same magnitude as the variance across the reference materials, requires large carbon abundances. However, the compositional variability within this catalogue greatly exceeds that which is expected within a MIXS footprint or a Mercurian terrane. Within sec-

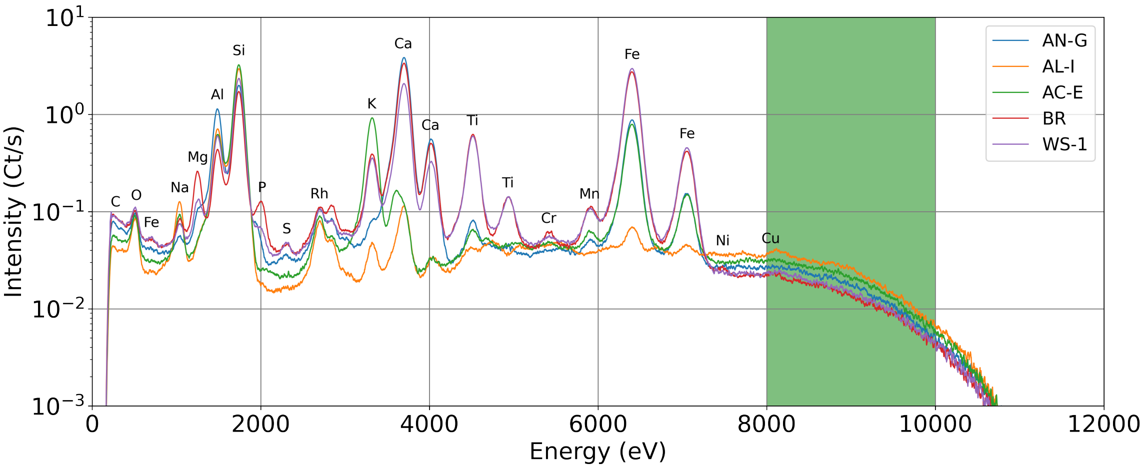

(a) Laboratory measured spectra from some of the reference materials in the sample catalogue.

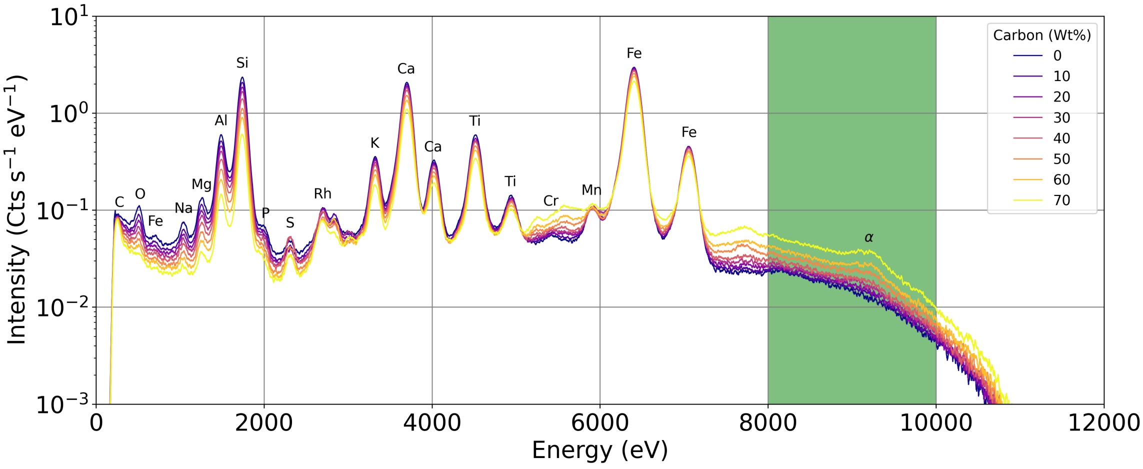

(b) Laboratory measured spectra from the sample series spiked with increasing graphite content.

Figure 5. Spectra from the MIXS Ground Reference Facility, taken at $\theta = 30^\circ$, $\phi = 0^\circ$ with the X-ray source operating at 10 kV. Green region highlights the energy range analysed for scatter intensity (8.00–10.00 keV).

tion 4, we directly investigate MIXS' ability to resolve these scatter changes against compositional variability in the underlying geochemical terranes.

The modelled results demonstrate good agreement with the observed values, giving confidence in the predictive capabilities of the model. We observe an under-prediction from the model for high carbon content samples, notably $>\sim$40 wt% and increasing thereafter. We attribute this largely to the rise the diffraction peak mentioned above, however, poorly constrained fundamental parameters for carbon could also contribute; there are believed to be larger uncertainties for low atomic number elements (Brunetti et al. 2004; Hall 2022).

4 PREDICTED MIXS OBSERVATIONS

4.1 Method

With confidence in the predictive model, from laboratory verification, we now simulate observations of LRM with the scatter analysis technique of Section 2.4. We use these predictions to assess the plausibility of the method for providing evidence for/against the presence of localized carbon enrichments. In this process we continue to evaluate Equation 10 with various solar-like incidence spectra and predicted Mercury compositions. The scatter intensities are predicted, as observed by the spacecraft with various levels of carbon enrichment. We also consider the co-addition of spectra acquired during multiple flare events and the sensitivity to carbon in that case.

4.1.1 Input Solar Spectrum

The solar spectrum is extremely temporally variable in both intensity and spectral shape. Flare events rapidly release large quantities of energy, during which the X-ray spectrum 'hardens' (increases intensity at higher energy relative to low) during flares with higher temperature plasma in the active region. The composition of the emitting plasma also determines the emission lines within that spectrum. Variations in the incident spectral shape means that the scattered light can have differing contributions from Rayleigh and Compton scatter, making co-addition of multiple observations challenging.

As the region of interest is at relatively high energy, the expected count rates in the incident, and by extension, detected spectra are negligible at those energies during quiescent periods. Thus, solar flares are required to utilise our methodology. We therefore model the count rates from best-fitting spectra to a variety of solar flares in

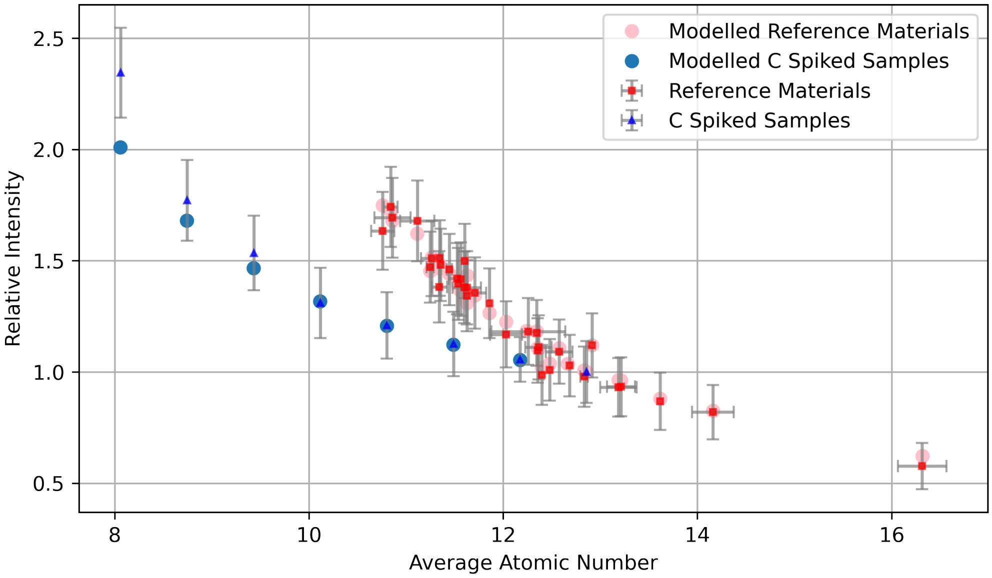

Figure 6. The observed and modelled scatter intensities between 8.000 and 10.000 keV in GReF observations of the reference material catalogue (red/pink) and graphite spiked samples (blue). Experimental results and modelled results have independently been normalized to the measurement of WS-1.

order to estimate the integration times required, under each of these conditions, to resolve the effect of carbon addition.

For these predictions, we sample five solar flares which were observed by the MESSENGER spacecraft during its over 4 year orbital phase around Mercury. We have selected these spectra on the basis of using the best-fitting plasma temperature as a proxy for flare magnitude. Using the fit data provided by Nittler et al. (2020), we identify the highest temperature flare event, as well as the 90th, 75th, 50th and 25th percentile. It should be noted that MESSENGER operated across a weak solar maximum and BepiColombo is currently anticipated to observe more frequent and more intense flares (see Section 4.3).

For each of these events, we have fitted to the calibrated data records (Starr 2018) from MESSENGER's SAX (Solar Assembly for X-rays) to derive a representative incident spectrum. We use the *CHIANTI* code (Version 10.1) (Dere et al. 1997; Del Zanna et al. 2021; Dere et al. 2023) as was used in MESSENGER analyses, described in detail by Nittler et al. (2011); Weider et al. (2014), to generate representative solar spectra at high (1 eV) resolution. We first convolve the *CHIANTI* output with a model of the SAX quantum efficiency (generated using Xraylib parameters) as well as a Gaussian with FWHM (full-width at half-maximum) derived from the telemetered SAX detector temperature according to the relation reported by Starr et al. (2016) and corrected for the illumination angle onto the SAX detector. We then use a least-squares fitting technique to optimize the fit for solar temperature and emission measure to SAX data. The fitting routine is applied to data in the range of 1.5 to 9 keV. The best-fitting parameters are then used to generate a high resolution (1 eV) input spectrum from which to calculate the scatter. The details of the flare events investigated, as well as the temperature fits, are given in Table 4.

A limitation of these spectral fits is that the solar plasma composition has not been varied; we instead use the coronal abundance estimates reported by Dere et al. (2023) and available in *CHIANTI*. The fits are also isothermal fits, as were the reported fits from MESSENGER XRS data, however Dennis et al. (2015) demonstrated that the multi-thermal fitting with a differential emission measure is necessary for interpreting specific XRF spectra. The development of the MIXS solar spectral fitting routine is ongoing and these limitations are being addressed as part of that process.

4.1.2 Mercury Compositions

The model projects the above solar illumination onto a surface of a Mercury-like composition. Multiple compositions are evaluated to represent different Mercurian surface terranes and are evaluated with both a base level of carbon and an enriched carbon content to represent LRM produced by mixing of graphite with overlying surface material. The terrane compositions are taken from the absolute abundances reported by Peplowski & Stockstill-Cahill (2019), in particular the chosen terranes are:

(i) 'Rachmaninoff Basin'
(ii) 'Low-Mg North'
(iii) 'Intermediate High-K'

Rachmaninoff is chosen on the basis of being a well constrained, localized area around which we anticipate one of the strongest LRM deposits on Mercury (Klima et al. 2018) and as such represents the greatest opportunity for this work. The Low-Mg Northern terrane is one composition existing within the Borealis Planitia, a region which has been inferred to makeup the opposing end-member to the LRM (Murchie et al. 2015). Lastly, the intermediate high-K terrane is chosen as it represents 'intermediate' values among Mercury compositions of Mg/Si and Al/Si, albeit with enriched K content.

4.1.3 Model Approach

4.1.3.1 Single Observation We model observations from both MIXS-T and MIXS-C from Mercury orbit with the illuminating spectra of Table 4, the compositions of Section 4.1.2 and a fixed geometry of $\theta = 30°$, $\phi = 0°$. The footprints of MIXS-T and MIXS-C will change with altitude, however, a given composition, the flux to the detector is scale invariant. Table 5 shows the scale of the footprints evaluated at various points in the orbit.

Table 4. Solar flare events used in this work with temperature fits as reported by Nittler et al. (2020) and as produced with our fitting routine. Flares classes as reported by the GOES-15 spacecraft (Machol et al. 2022) where available. Bracketed values with GOES classification represent angular separation between Earth and Mercury from the Sun. The event of 26 Dec 2013 is not classified as it was not well observed by GOES-15.

Start Date/Time (UT)	Integration Time (s)	Temperature (MK)	Our Temperature (MK)	GOES Flare Class	Heliocentric Distance (AU)
2014/10/16 12:56:39	20	37.34	32.95	M6.2 (3.5°)	0.33
2012/10/09 23:25:44	40	20.73	19.66	M2.4 (114.5°)	0.47
2014/10/14 20:30:14	20	16.93	15.87	M3.3 (9.5°)	0.34
2012/06/13 19:23:33	450	14.13	14.08	C9.7 (98.2°)	0.37
2013/12/26 02:57:30	2000	12.12	12.72	N/A (172.8°)	0.46

Table 5. MIXS instrument footprints at various points in the orbit, units are km. Singular MIXS-T detector pixels represent 1 arc min, the values in this case are pixel edge lengths, these pixels are unresolved by the optic which has a FWHM of ~9 arc min.

	Apoherm	Semi-Major Axis	Periherm
MIXS-T Detector Pixel	0.451	0.295	0.140
MIXS-T Total Footprint Diameter	28.857	18.897	8.936
MIXS-C Footprint Diameter	271.215	177.602	83.989

For each terrane and solar spectrum, the incident X-ray flux is calculated by multiplying the modelled *CHIANTI* spectrum by the ratio of pixel footprint area (determined by instrument and altitude) to the area of the SAX detector window. We have then generated 3600 individual compositions to replicate variability in each terrane. For each sample composition, the abundance of each element is sampled from a Gaussian distribution; those distributions have means and standard deviations corresponding to the values reported in Peplowski & Stockstill-Cahill (2019). Once all elements have been sampled, the overall composition is re-normalized to 100 wt%.

The modelled scatter intensity can now be calculated for each sample composition through Equation 10; we evaluate this with dE =10 eV. This includes multiplication by the effective solid angle of the instrument as seen from the surface, set by the altitude of the spacecraft and the effective area of the optic. The effective area of MIXS-T at this energy is approximated at 5 cm^2, extrapolated from the on-axis results reported by Fraser et al. (2010). For MIXS-C the effective area is 0.768 cm^2, this is calculated as an average of the effective area from each off-pointing angle, weighted by the contributing footprint areas at each angle. The effective area as a function of angle is constant at 1.4 cm^2 over the central 3.25° off-axis and decreases linearly to zero at 5.2°.

This process is evaluated twice, firstly for the background terrane; here a base level of carbon of 1 wt% is added prior to re-normalisation, representing a global level which is consistent with estimations by Peplowski et al. (2015, 2016). Secondly, the same compositions are calculated with the addition of a further 4 wt% carbon before re-normalisation. This is consistent with the strongest deposits of LRM (Peplowski et al. 2016; Klima et al. 2018), which present the greatest opportunity to make these measurements. We histogram the distributions produced by modelled LRM and non-LRM material to estimate the flux required to resolve differences between the two populations and the integration times this demands.

We also test higher abundances of carbon to predict the integration times required to identify upper limits. We model up to 12 wt% enrichments, in these cases we model only the Rachmaninoff composition with the highest temperature flare.

We do not include the effect of detector quantum efficiency or attenuation by optical blocking filters, since, at these energies, the detector QE is ~100% (Majewski et al. 2014) and transmission through the filters is >99%, meaning any reduction to the count rates will not be significant.

4.1.3.2 Multiple Observations

In order to achieve the counting statistics required to meet a particular level of sensitivity, we may wish to combine observations of the same region. By nature, the incident solar spectrum will be different for two or more observations and, as described previously, this complicates analyses. We investigate the inherent uncertainty produced on estimation of carbon enrichment by inference from the ratio of scattered flux to incident flux for co-added spectra. The input spectra for this are also modelled solar spectra from *CHIANTI* fits to real SAX data from the MESSENGER mission. We fit to the 10 continuous flare events in the catalogue of Nittler et al. (2020) which have the highest maximum flare temperature, giving 224 individual, non-overlapping spectra from which to sample.

We model 100,000 combinations of spectra. Each combination comprises a random number of flares between 1 and 5. Each flare is taken from the 224 generated best-fitting *CHIANTI* spectra and is assigned a random duration between 20 and 40 seconds. For each flare in a combination, we model the interactions with the same base composition, Rachmaninoff +1 wt% carbon, and then add a random carbon enrichment of between 0 and 8 wt%. This generates a large and continuous dataset with which to empirically identify the trends with carbon content and with flare temperature.

We quantify each combination with an average flare temperature, taken as the count-weighted average of the plasma temperatures of each flare spectrum from which it is constituted. An empirical fit with a third order polynomial is then used to correct for the effects of average flare temperature on the measured ratio. By linear regression between the new, corrected ratio and carbon enrichment, we can make predictions of carbon enrichment from a measurement of this quantity alone. In this work, we evaluate the residuals between the inferred carbon content and 'real' carbon content. Changes in plasma composition also affect these results and is an unavoidable challenge when combining observations taken during multiple flares, which perhaps emanate from different active regions. These differences can be accounted for, however, this requires good knowledge of the composition of the active region. Most importantly to this work, the Fe and Ni abundances should be well characterized as they produce emission lines within our region of interest (Phillips 2004). Again, planned development of the MIXS solar fitting routine will address this.

4.2 Modelling Results

A sample solar spectrum used as an input into the modelled MIXS observations is displayed in Figure 7. The 'true', observed data from SAX is shown, along with the best-fit modelled spectrum in the fitting range (1.5-9 keV). These spectra feature an overturn at ~2 keV, below which Be filters attenuate the incident X-ray flux. The major feature of the spectrum is the Fe peak complex around 6.7 keV; this and other smaller peak complexes sit atop a steep continuum. The high-resolution spectrum which produces the SAX modelled curve and which is ultimately used as the input for MIXS simulations is also shown, with sharp emission lines throughout.

4.2.1 Single Observation

We present a select few histograms here which are representative of the core range of scenarios which have been explored for single flare analysis (Figure 8). These histograms, fitted with Gaussian distributions, display the dispersion of scatter intensity caused by simulated variability in the composition of the underlying terrane.

In Figures 8a and 8b the difference in flux received by a MIXS-T detector pixel and the flux collimated by MIXS-C can be observed. MIXS-T gives the option of combining pixels to obtain higher count rates (at the expense of spatial resolution). However, even summing over all illuminated pixels, the integrated count rate for this energy range is ~15× lower than for MIXS-C.

Distributions of MIXS-C intensities are shown in Figures 8c, 8d and 8e for the three different terranes under illumination from the highest temperature solar flare of the MESSENGER mission as reported by Nittler et al. (2020). The separation of the means between 0 and 4 wt% carbon enriched material, expressed in number of standard deviations, was found to be very consistent for a given composition across all incidence spectra. These results are shown in Table 6.

The separation, in standard deviations, is greatest for the Rachmaninoff terrane, which can be attributed to having narrower distributions. These are lowest for the Rachmaninoff composition as this has the smallest variance in the composition of background (non-carbon) material, most critically in Ca. Calcium is the second heaviest element included and is significantly more abundant than Fe, as such a large proportion of the interactions take place in Ca atoms, meaning large variability in its abundance creates wide distributions in scattered X-ray intensity. In the case of the Northern Low-Mg terrane, this effect broadens the distributions to the point at which the means are only separated by $\sim 1\sigma$.

Considering the percentage difference between the means of the two populations (Table 6), we calculate the number of counts required to produce a matching uncertainty considering only Poisson statistics. Combining these required total counts with the mean intensities, we estimate the required integration times, for each considered flare, to statistically resolve the two populations, this is displayed in Table 7.

Notably, the required integration times for the 90th percentile flare are higher than for the 75th percentile flare. This result highlights a limitation of ranking by the temperature of the solar fits. The emission measure in the fit to the 90th percentile flare is ~5× lower than that of the 75th percentile flare, the effect of this outweighs the hardening effect of the spectrum in this case, this is also reflected in the GOES flare classifications for these flares in Table 4.

The count rates, separation of means and derived resolving integration times produced for higher carbon abundances are shown in Table 8.

4.2.2 Multiple Observations

Modelled ratios of detected flux to incident flux for different combinations of flares are shown in Figure 9, colour coded by carbon content. The ratios demonstrate a clear correlation with plasma temperature, which is fitted with a polynomial. Note that the absolute magnitude of the ratio is related to geometric factors of the MIXS-C field of view and effective area; the ratio reflects the X-rays collected by MIXS compared to the incident flux over the entire observation footprint. It is clear that the effects of flare temperature dominate over the increase in measured ratio caused by increases in carbon content. However, increasing carbon content does systematically increase the ratio, which can be seen more clearly following temperature correction using the fitted polynomial (Figure 10).

With the linear fit between carbon enrichment and temperature-corrected ratio (shown in Figure 10), predicted carbon enhancements can be derived directly from the corrected ratios. The residuals between the 'predicted' and true carbon enrichment are displayed in Figure 11 against flare temperature; this figure also shows the means and standard deviations for data in each 2 MK temperature bin. In all cases except the highest temperature bin the mean lies within one standard deviation of zero, however the histogram hints that some underlying temperature-related structure persists in the data.

4.3 Discussion of Models

Our predicted count rates first find that MIXS-T, whose design is not optimized for high-energy observations, does not yield ample count rates for this technique to resolve enrichments of carbon at anticipated abundances. Even when the entire detector array is combined, in the best case of Rachmaninoff composition with the highest temperature solar flare, the estimated integration time required is >1400 seconds. Therefore, plausible methodologies all relate to use of MIXS-C, herein we will only consider MIXS-C observations.

Before considering the limits on abundance resolvability due to overall counting statistics, we consider the variability induced from compositional variation (excluding carbon) within each terrane. As described in Section 4.2.2, the Rachmaninoff composition exhibits the smallest distributions of scatter intensities within each (carbon-free/carbon-bearing) population, owing to having the lowest standard deviations in abundances reported by Peplowski & Stockstill-Cahill (2019). The broader scatter distributions for other terranes, created by Ca variability may be attributed to the larger spatial areas which contribute to each terrane classification. In the context of our proposed method, we note that any acquired data which meets the requirements for scattered counts at high energy, will also have high fluorescence counts from all major elements up to and including Fe. This means that the major element composition of the region being analysed will be well constrained and the corresponding compositional variability will be reduced. As a result, an increase in sensitivity may be possible in practice over that modelled here which uses the bulk terrane compositional variation.

The integration times reported in Table 7 show that under some of the most energetic solar flares observed by MESSENGER, measurements using this technique are plausible. The integration times of

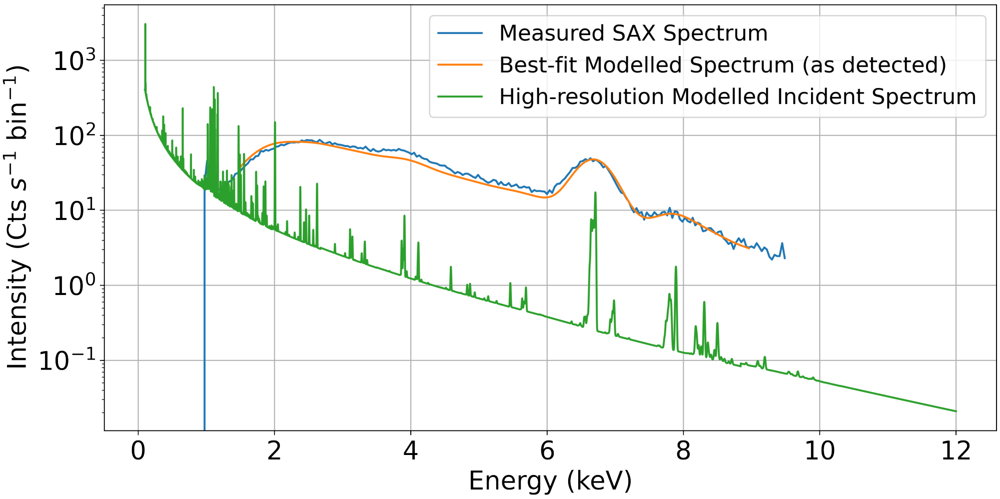

Figure 7. Best fit to the 2014/10/16 solar flare. Showing real SAX data (blue), best-fitting modelled data convolved with SAX response (orange) and raw, high-resolution best-fitting modelled data (green).

Table 6. Separation of the means for 0 and 4 wt% carbon enrichment in different scenarios, expressed in % of the 0 wt% mean and $n\sigma$ of the 0 wt% population in brackets. Values taken from the MIXS-C model.

Flare Temperature Percentile	Rachmaninoff	Northern Low-Mg	Intermediate High-K
25	2.18 (3.76)	2.16 (0.97)	2.17 (2.12)
50	2.20 (3.69)	2.17 (1.00)	2.18 (2.12)
75	2.21 (3.77)	2.18 (1.01)	2.20 (2.13)
90	2.25 (3.82)	2.22 (1.02)	2.24 (2.16)
100	2.34 (3.96)	2.31 (1.03)	2.33 (2.21)

Table 7. Estimated integration times required to statistically resolve the difference in scatter intensity between 0 and 4 wt% additional carbon to 1σ. Values are in seconds and taken from the MIXS-C model.

Flare Temperature Percentile	Rachmaninoff	Northern Low-Mg	Intermediate High-K
25	67,591	71,612	69,344
50	45,778	48,554	46,957
75	2,625	2,782	2,693
90	4,646	4,927	4,765
100	267	282	273

hundreds of seconds are consistent with the duration of peak activity for energetic solar flares (~tens of minutes) and are operationally viable. The scatter intensity is similar in magnitude for each of the terranes and thus the integration time is not greatly different for the same carbon enrichment. This, combined with knowledge of the major element composition, potentially opens up different targets across the surface in addition to the preferred Rachmaninoff ejecta. However, such high carbon enrichments are not currently anticipated on large spatial scales elsewhere on Mercury's surface (Klima et al. 2018).

The integration periods we consider show the value of carrying out targeted 'stare' observations of an LRM rich region and a region of surrounding terrane. Such 'stare' campaigns are planned for BepiColombo's extended mission but will naturally involve collecting over a range of emergence angles. The exact angles involved may have to be interpreted post the data collection. MIXS-C data is telemetered as time-tagged histograms, nominally every 3 seconds. This allows the opportunity to temporally bin data at chosen points in analysis once a desired number of counts have been recorded. MESSENGER also carried out targeted observations to maximize the chance of coinciding with a solar flare, this was successful in one notable case, providing high-quality data from North-East of Rachmaninoff (Weider et al. 2016).

The frequency of solar flares is logarithmic with intensity, lower class (and typically lower temperature) flares occur exponentially more frequently than more intense flares. Therefore, suitably energetic solar flares to enable these observations are rare, however, there are perhaps more opportunities than the MESSENGER list implies. The MESSENGER spacecraft had pointing requirements that prevented XRS' bore sight from always intercepting the surface, since the catalogue of Nittler et al. (2020) considers only solar flares with associated XRS spectra, some solar flares are undoubtedly excluded. As BepiColombo is not subject to the same constraints, MIXS will always be intercepting the surface and gathering suitable data when on the day-side. Lastly, BepiColombo will arrive at Mercury shortly after solar maximum (Labonville et al. 2019; Bunce et al. 2020), a

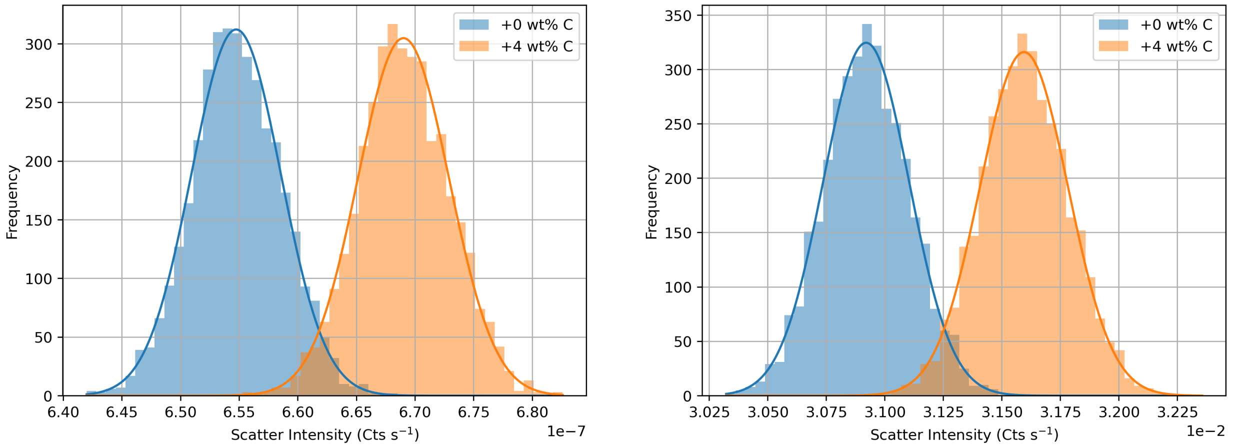

(a) Rachmaninoff Basin Terrane, 25th percentile flare, MIXS-T, per pixel.

(b) Rachmaninoff Basin Terrane, 25th Percentile Flare, MIXS-C.

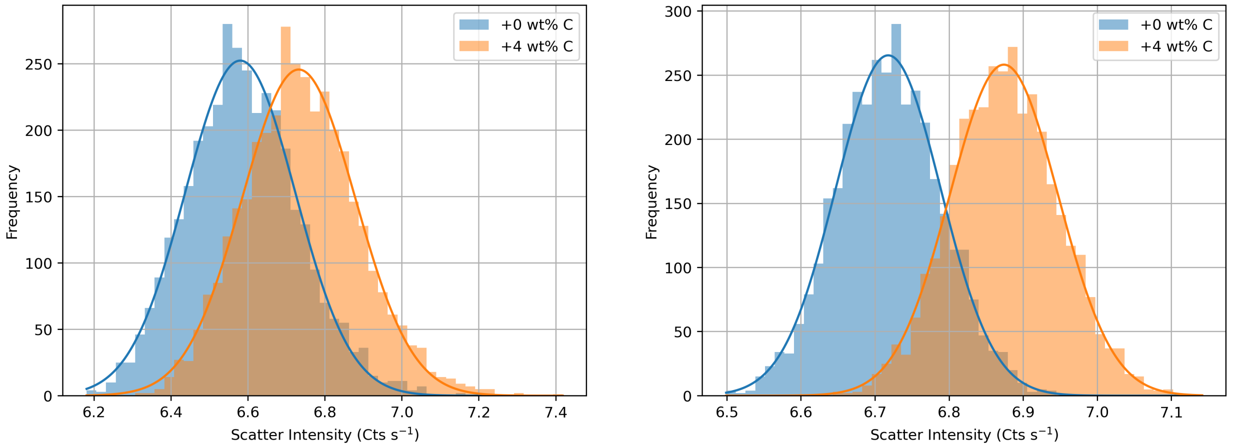

(c) Northern Low-Mg Terrane, 100th Percentile Flare, MIXS-C.

(d) Intermediate High-K Terrane, 100th Percentile Flare, MIXS-C.

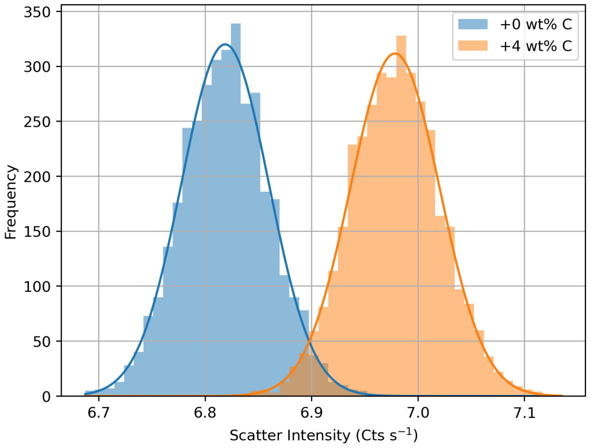

(e) Rachmaninoff Basin Terrane, 100th Percentile Flare, MIXS-C.

Figure 8. Histograms of scatter intensity measured by MIXS in the energy range 8.00–10.00 keV, modelled from different Mercury terranes and under differing solar conditions. $\theta = 30°$, $\phi = 0°$. Note the varying orders of magnitude in scatter intensity between certain plots.

period when solar flares are expected to occur with both elevated frequency and intensity. Solar cycle 24, during which MESSENGER orbited Mercury was a weak solar maximum, with solar cycle 25 having already recorded higher sunspot numbers (e.g. Clette & Lefèvre (2015)). These factors lead to the suggestion that MIXS may be in operation during more and higher temperature solar flares than MESSENGER, aiding our methodology. Analysis of higher carbon abundances suggest that providing an upper limit on carbon enrichments in regions of LRM will be possible under less demanding solar conditions.

The results for combining solar flares provide an indication that this too may be a suitable method to provide carbon enrichment esti-

Table 8. MIXS-C modelled results between 8.00 and 10.00 keV for Rachmaninoff composition with varied excess carbon. Modelled for 16 Oct 2014 flare, $\theta = 30°$, $\phi = 0°$.

Carbon Enrichment (wt%)	Mean Count Rate (s^{-1})	Separation of Means ($\%/\sigma$)	Required Integration Time (s)
4	7.00	2.34/3.96	267
5	7.04	2.96/4.95	167
6	7.08	3.58/5.99	114
8	7.17	4.87/8.15	62
10	7.26	6.20/10.38	38
12	7.36	7.59/12.71	25

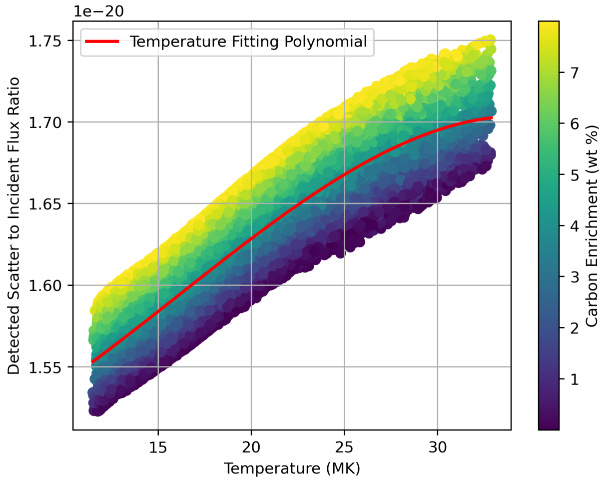

Figure 9. Ratio of detected scattered X-ray intensity to incident surface flux in the MIXS-C FOV, plotted against count-weighted average flare temperature for modelled observations of carbon enriched material. Flares have a fixed ('Coronal') plasma composition. Red line shows the empirically fitted third-order polynomial that is used to approximate the response of changing temperature on the ratio.

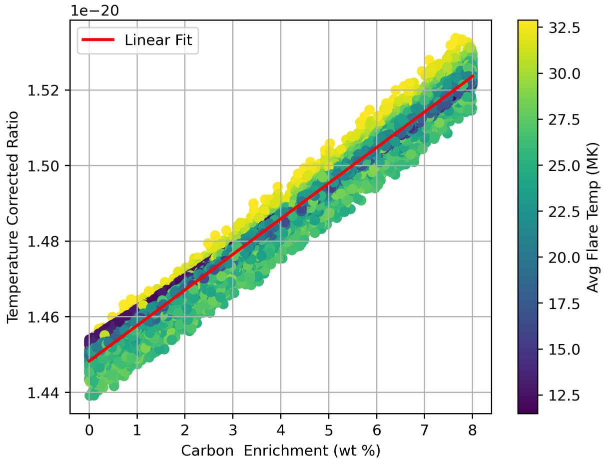

Figure 10. The correlation with carbon enrichment in modelled data of the ratios in Figure 9 following a plasma temperature correction. Colours here represent the average emitting plasma temperature and the solid red line indicates the linear best-fit (later used to predict carbon content)

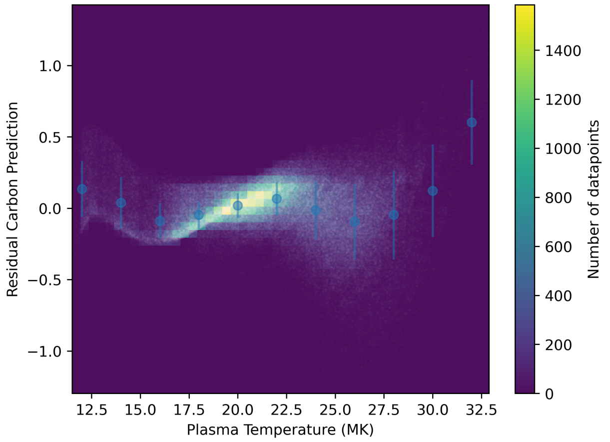

Figure 11. Residuals between the true carbon enrichment which is an input to the calculation and the carbon enrichment predicted by the temperature corrected ratio. White circles show each of the 100,000 modelled observations. A 2D histogram of the residuals is overlain, whilst the blue points display local means and standard deviations in 2 MK wide temperature bins.

mations where exceptionally large solar flares are not observed over a target region. For a given solar plasma composition, carbon enrichment estimates have an inherent uncertainty of ± <1 wt%, in addition to the uncertainty of the achieved counting statistics. However, when combining measurements taken from flares with different plasma composition, this uncertainty can increase greatly. High confidence in solar fits will be required to utilise this method. In particular, good fitting of the Fe and Ni abundances in the emitting plasma is important, as these elements contribute emission lines to our identified energy window.

5 COMBINED OUTLOOK OF EXPERIMENTATION AND MODELLING

Through Section 3, we have determined that our scatter-based approach to identifying carbon (or low-Z) enrichments is a viable methodology. We demonstrate the ability to accurately model the observations we make in a laboratory environment. Using this model, we have estimated the integration times required to resolve carbon-enhanced material at Mercury. The results, presented in Section 4 determine that single observations with energetic solar flares can resolve anticipated carbon abundances with integration times that are achievable. We have also identified that combining multiple observations may be suitable if adequate solar conditions are not achieved.

5.1 Additional Considerations

Some final considerations for application of this technique include that there is likely one other candidate which could significantly increase the scattered X-ray intensity, oxygen. Modelled results show that an absolute increase in oxygen abundance of ~2× that of carbon would produce a similar level of scattering increase in the <+10 wt% region (see Supplementary Figure 1). Verification of the oxygen abundances through the fluorescence spectrum, directly and/or via stoichiometry are therefore important. Oxygen fluorescence can, however, be observed even under quiescent solar conditions. Direct determination of the oxygen abundance is challenging for similar reasons to carbon: limited knowledge of the incident spectrum at low energy and a requirement to lower the instrument event threshold.

The results we model here assume a compositionally homogenous sample with a smooth surface. In modelling observations of laboratory samples, this assumption is valid, however there may be additional considerations for orbital observations, particularly when crossing geochemical boundaries or extreme topography.

Lastly, in principle, the identified energy window includes the Ir L series, beginning at 9.175 keV which may be excited as self-fluorescence from reflective coatings on the MIXS optic. The absorption edge for this emission is at 11.215 keV and as such will only be triggered by scattered X-rays in which case fluorescence will be extremely low intensity, or more significantly by energetic particles. Particle induced X-ray fluorescence was also observed by MESSENGER's XRS (e.g. Ho et al. (2011)) and is expected to only occur at specific points (predominantly magnetic-cusps) on select orbits.

With consideration of these effects, we determine that this methodology has the potential to be applied during orbital operations of the BepiColombo mission. In the following section we outline our proposed methodology for carrying out these observations and analyses.

5.2 Final Proposed Methodology

We determine the most suitable application of our technique, which maximizes the carbon sensitivity, to be as follows.

Spectra from the wide field of view, collimating, MIXS-C will be combined to produce long integration spectra. The scattered X-ray intensity, measured across 8.00–10.00 keV, will be summed. If there is evidence of instrumental self-fluorescence, identified by Ir L line fluorescence, the upper energy limit may be reduced. These observations would be further supported with dedicated 'stare' campaigns during BepiColombo's extended mission, as were successfully utilised by MESSENGER (Weider et al. 2016). One key target is the Rachmaninoff basin ejecta, with smaller scale targets including the Basho and Atget impact craters. To resolve predicted changes in scatter intensity for these regions, serendipitous occurrences of energetic solar flares are required. Two separate integrations are necessary, one which targets a region believed to be LRM-rich and another of surrounding material.

The major element compositions for these regions will be derived from the spectra by the conventional MIXS method of analysing the fluorescence lines. Using this information, forward modelling with varying levels of carbon content, as has been shown here, can place an estimation on carbon enrichment through relative differences in the scatter intensities. Consideration of the rapidly changing solar incidence spectrum following a solar flare peak is likely to be required. The total integrated counts for each region will be the determining factor for the level of sensitivity to carbon that this method provides.

In the absence of a single suitably large solar flare, observations taken during multiple, smaller flares may be combined. This requires good knowledge of the solar plasma composition, a routine for which is in development, as well as application of a correction for plasma temperature. Combining flares also requires consideration of changing observation geometry and the most suitable analysis will be determined by the data which is returned in practice.

6 SUMMARY

We identify a new method for observing the effects of carbon enrichment in LRM relative to surrounding material of similar composition using MIXS. These effects are observed as an increase in scattered X-ray intensity, most notably at energies higher than 7.2 keV (the Fe K absorption edge). We have made laboratory measurements using a flight qualified MIXS detector and samples of known composition to physically verify these effects and validate a predictive model. We have then used that model to evaluate the conditions required to make these measurements with MIXS from Mercury orbit and resolve carbon-rich from non-carbon-rich material.

Our modelled results show that low variability in the overlying terrane is required, particularly in heavy rock forming elements (e.g. Ca, Fe). However, such variability is not unexpected for well constrained, regions of Mercury and the exact major element composition of the areas observed will be well characterized from the fluorescence signal. We find that energetic solar flares are a requirement for making these measurements, however this analysis would greatly benefit from targeted 'stare' observations, involving targeted pointing for several minutes. Application of our methodology will be restricted only to observations with MIXS-C, for which the footprint ranges between ~84 and 270 km.

The sensitivity to carbon will ultimately be determined by the total number of counts recorded in the energy range. With integration times of hundreds of seconds under energetic solar flares, 1σ resolution may be achieved for carbon enrichments of ~4 wt%. This leads us to propose targeted observations of regions believed to be strongest in LRM, including Rachmaninoff basin ejecta to maximize the likelihood serendipitous flare activity. The required integration time rapidly decreases for increasing carbon abundance and higher upper limits (e.g. 6-8 wt%) are more easily achieved. Through combining observations, similar capabilities may be achievable through multiple, smaller solar flares, however, this invokes additional uncertainty (±>0.5 wt%) and requires good knowledge of the emitting solar plasma for each flare.

ACKNOWLEDGEMENTS

We thank Lin Marvin for assistance and guidance during sample preparation. The development of the MIXS Ground Reference Facility was funded by the UK Space Agency (UKSA) and the University of Leicester. Adam Fox is funded by the Future 100 PhD scheme at the University of Leicester. The MIXS team is a large international consortium of institutes, at the University of Leicester they are funded by UKSA, STFC and ESA. This research used the ALICE High Performance Computing facility at the University of Leicester. This work uses the CHIANTI atomic database and code, CHIANTI is a collaborative project involving George Mason University, the University of Michigan (USA), University of Cambridge (UK) and NASA Goddard Space Flight Center (USA). ON acknowledges support from the European Research Council (ERC) for a Consolidator Grant (IronHeart) under the European Union's Horizon (grant agreement no. 101125126) and from the ESA PRODEX Program (Grant

4000142722). Views and opinions expressed are however those of the author(s) only and do not necessarily reflect those of the European Union or KU Leuven. Neither the European Union nor the granting authority can be held responsible for them. For the purpose of open access, the author has applied a Creative Commons Attribution (CC BY) licence to the Author Accepted Manuscript version arising from this submission.

DATA AVAILABILITY

This work made use of SAX data from the MESSENGER mission which is available through NASA's Planetary Data System at the PDS Geosciences Node at `https://pds-geosciences.wustl.edu/messenger/mess-e_v_h-xrs-3-cdr-spectra-v1/` (Starr 2018). This work uses the CHIANTI atomic database, the Xraylib database, and the GeoRem database, the sources of which are referenced in the text. This work also uses flare summary data products from the GOES-15 satellite, provided by NOAA-NCEI and available at: `https://www.ncei.noaa.gov/data/goes-space-environment-monitor/access/science/xrs/goes15/xrsf-l2-flsum_science/`. Any additional data underlying this article is available by request to the corresponding author.

REFERENCES

Barraud, O., Doressoundiram, A., Besse, S., & Sunshine, J., 2020. Near-ultraviolet to near-infrared spectral properties of hollows on Mercury: Implications for origin and formation process, *Journal of Geophysical Research: Planets*, **125**(12), e2020JE006497.

Barraud, O., Besse, S., & Doressoundiram, A., 2023. Low sulfide concentration in Mercury's smooth plains inhibits hollows, *Science Advances*, **9**(12), eadd6452.

Benkhoff, J., Murakami, G., Baumjohann, W., Besse, S., Bunce, E., Casale, M., Cremosese, G., Glassmeier, K.-H., Hayakawa, H., Heyner, D., Hiesinger, H., Huovelin, J., Hussmann, H., Iafolla, V., Iess, L., Kasaba, Y., Kobayashi, M., Milillo, A., Mitrofanov, I. G., Montagnon, E., Novara, M., Orsini, S., Quemerais, E., Reininghaus, U., Saito, Y., Santoli, F., Stramaccioni, D., Sutherland, O., Thomas, N., Yoshikawa, I., & Zender, J., 2021. BepiColombo-mission overview and science goals, *Space science reviews*, **217**(8), 90.

Blewett, D. T., Robinson, M. S., Denevi, B. W., Gillis-Davis, J. J., Head, J. W., Solomon, S. C., Holsclaw, G. M., & McClintock, W. E., 2009. Multispectral images of Mercury from the first MESSENGER flyby: Analysis of global and regional color trends, *Earth and Planetary Science Letters*, **285**(3-4), 272–282.

Blewett, D. T., Chabot, N. L., Denevi, B. W., Ernst, C. M., Head, J. W., Izenberg, N. R., Murchie, S. L., Solomon, S. C., Nittler, L. R., McCoy, T. J., Xiao, Z., Baker, D. M. H., Fassett, C. I., Braden, S. E., Oberst, J., Scholten, F., Preusker, F., & Hurwitz, D. M., 2011. Hollows on Mercury: MESSENGER evidence for geologically recent volatile-related activity, *Science*, **333**(6051), 1856–1859.

Blewett, D. T., Vaughan, W. M., Xiao, Z., Chabot, N. L., Denevi, B. W., Ernst, C. M., Helbert, J., D'Amore, M., Maturilli, A., Head, J. W., & Solomon, S. C., 2013. Mercury's hollows: Constraints on formation and composition from analysis of geological setting and spectral reflectance, *Journal of Geophysical Research: Planets*, **118**(5), 1013–1032.

Blewett, D. T., Stadermann, A. C., Susorney, H. C., Ernst, C. M., Xiao, Z., Chabot, N. L., Denevi, B. W., Murchie, S. L., McCubbin, F. M., Kinczyk, M. J., Gillis-Davis, J. J., & Solomon, S. C., 2016. Analysis of MESSENGER high-resolution images of Mercury's hollows and implications for hollow formation, *Journal of Geophysical Research: Planets*, **121**(9), 1798–1813.

Bruck Syal, M., Schultz, P. H., & Riner, M. A., 2015. Darkening of Mercury's surface by cometary carbon, *Nature Geoscience*, **8**(5), 352–356.

Brunetti, A., Del Rio, M. S., Golosio, B., Simionovici, A., & Somogyi, A., 2004. A library for X-ray–matter interaction cross sections for X-ray fluorescence applications, *Spectrochimica Acta Part B: Atomic Spectroscopy*, **59**(10-11), 1725–1731.

Bunce, E. J., Martindale, A., Lindsay, S., Muinonen, K., Rothery, D. A., Pearson, J., McDonnell, I., Thomas, C., Thornhill, J., Tikkanen, T., Feldman, C., Huovelin, J., Korpela, S., Esko, E., Lehtolainen, A., Treis, J., Majewski, P., Hilchenbach, M., Väisänen, T., Luttinen, A., Kohout, T., Pentillä, A., Bridges, J., Joy, K. H., Alcacera-Gill, M. A., Alibert, G., Anand, M., Bannister, N., Barcelo-Garcia, C., Bicknell, C., Blake, O., Bland, P., Butcher, G., Cheney, A., Christensen, U., Crawford, T., Crawford, I. A., Dennerl, K., Dougherty, M., Drumm, P., Fairbend, R., Genzer, M., Grande, M., Hall, G. P., Hodnett, R., Houghton, P., Imber, S., Kallio, E., Lara, M. L., Margeli, A. B., Mas-Hesse, M. J., Maurice, S., Milan, S., Millington-Hotze, P., Nenonen, S., Nittler, L., Okada, T., Ormö, J., Perez-Mercader, J., Poyner, R., Robert, E., Ross, D., Pajas-Sanz, M., Schyns, E., Seguy, J., Strüder, L., Vaudon, N., Viciera-Martín, J., Williams, H., Willingale, D., & Yeoman, T., 2020. The BepiColombo Mercury Imaging X-ray Spectrometer: science goals, instrument performance and operations, *Space Science Reviews*, **216**(8), 1–38.

Campbell, J., Perrett, G., Maxwell, J., Nield, E., Gellert, R., King, P., Lee, M., O'Meara, J., & Pradler, I., 2013. Refinement of the Compton–Rayleigh scatter ratio method for use on the Mars Science Laboratory alpha particle X-ray spectrometer, *Nuclear Instruments and Methods in Physics Research Section B: Beam Interactions with Materials and Atoms*, **302**, 24–31.

Cartier, C., Namur, O., Nittler, L., Weider, S., Crapster-Pregont, E., Vorburger, A., Frank, E., & Charlier, B., 2020. No FeS layer in Mercury? Evidence from Ti/Al measured by MESSENGER, *Earth and Planetary Science Letters*, **534**, 116108.

Cartwright, J. A., Martindale, A., Hall, G. P., Lindsay, S. T., Fox, A. R. D., McKee, M., & Bunce, E. J., 2025. Assessing Mercury's composition using GREF: The BepiColombo MIXS Ground REference Facility - in prep., *RAS Techniques and Instruments*.

Clette, F. & Lefèvre, L., 2015. SILSO Sunspot Number V2.0, Published by WDC SILSO - Royal Observatory of Belgium (ROB).

Cremonese, G., Capaccioni, F., Capria, M. T., Doressoundiram, A., Palumbo, P., Vincendon, M., Massironi, M., Debei, S., Zusi, M., Altieri, F., Amoroso, M., Aroldi, G., Baroni, M., Barucci, A., Bellucci, G., Benkhoff, J., Besse, S., Bettanini, C., Blecka, M., Borrelli, D., Brucato, J. R., Carli, C., Carlier, V., Cerroni, P., Cicchetti, A., Colangeli, L., Dami, M., Da Deppo, V., Della Corte, V., De Sanctis, M. C., Erard, S., Esposito, F., Fantinel, D., Ferranti, L., Ferri, F., Ficai Veltroni, I., Filacchione, G., Flamini, E., Forlani, G., Fornasier, S., Forni, O., Fulchignoni, M., Galluzzi, V., Gwinner, K., Ip, W., Jorda, L., Langevin, Y., Lara, L., Leblanc, F., Leyrat, C., Li, Y., Marchi, S., Marinangeli, L., Marzari, F., Mazzotta Epifani, E., Mendillo, M., Mennella, V., Mugnuolo, R., Muinonen, K., Naletto, G., Noschese, R., Palomba, E., Paolinetti, R., Perna, D., Piccioni, G., Politi, R., Poulet, F., Ragazzoni, R., Re, C., Rossi, M., Rotundi, A., Salemi, G., Sgavetti, M., Simioni, E., Thomas, N., Tommasi, L., Turella, A., Van Hoolst, T., Wilson, L., Zambon, F., Aboudan, A., Barraud, O., Bott, N., Borin, P., Colombatti, G., El Yazidi, M., Ferrari, S., Flahaut, J., Giacomini, L., Guzzetta, L., Lucchetti, A., Martellato, E., Pajola, M., Slemer, A., Tognon, G., & Turrini, D., 2020. Simbio-sys: Scientific cameras and spectrometer for the bepicolombo mission, *Space science reviews*, **216**, 1–78.

Del Zanna, G., Dere, K., Young, P., & Landi, E., 2021. CHIANTI—an atomic database for emission lines. XVI. Version 10, further extensions, *The Astrophysical Journal*, **909**(1), 38.

Denevi, B. W. & Robinson, M. S., 2008. Mercury's albedo from Mariner 10: Implications for the presence of ferrous iron, *Icarus*, **197**(1), 239–246.

Denevi, B. W., Robinson, M. S., Solomon, S. C., Murchie, S. L., Blewett, D. T., Domingue, D. L., McCoy, T. J., Ernst, C. M., Head, J. W., & Watters, T. R., 2009. The evolution of Mercury's crust: A global perspective from MESSENGER, *Science*, **324**(5927), 613–618.

Dennis, B. R., Phillips, K. J., Schwartz, R. A., Tolbert, A. K., Starr, R. D.,

& Nittler, L. R., 2015. Solar flare element abundances from the solar assembly for X-rays (SAX) on MESSENGER, *The Astrophysical Journal*, **803**(2), 67.

Dere, K., Landi, E., Mason, H., Fossi, B. M., & Young, P., 1997. CHIANTI-an atomic database for emission lines-I. Wavelengths greater than 50 Å, *Astronomy and Astrophysics Supplement Series*, **125**(1), 149–173.

Dere, K. P., Del Zanna, G., Young, P., & Landi, E., 2023. CHIANTI—An Atomic Database for Emission Lines. XVII. Version 10.1: Revised Ionization and Recombination Rates and Other Updates, *The Astrophysical Journal Supplement Series*, **268**(2), 52.

Elam, W. T., Ravel, B. D., & Sieber, J., 2002. A new atomic database for X-ray spectroscopic calculations, *Radiation Physics and Chemistry*, **63**(2), 121–128.

Evans, L. G., Peplowski, P. N., Rhodes, E. A., Lawrence, D. J., McCoy, T. J., Nittler, L. R., Solomon, S. C., Sprague, A. L., Stockstill-Cahill, K. R., & Starr, R. D., 2012. Major-element abundances on the surface of mercury: Results from the messenger gamma-ray spectrometer, *Journal of Geophysical Research: Planets*, **117**(E12).

Fraser, G., Carpenter, J., Rothery, D., Pearson, J., Martindale, A., Huovelin, J., Treis, J., Anand, M., Anttila, M., & Ashcroft, M., 2010. The Mercury Imaging X-ray Spectrometer (MIXS) on Bepicolombo, *Planetary and Space Science*, **58**(1-2), 79–95.

Goldsten, J. O., Rhodes, E. A., Boynton, W. V., Feldman, W. C., Lawrence, D. J., Trombka, J. I., Smith, D. M., Evans, L. G., White, J., Madden, N. W., Berg, P. C., Murphy, G. A., Gurnee, R. S., Strohbehn, K., Williams, B. D., Schaefer, E. D., Monaco, C. A., Cork, C. P., Del Eckels, J., Miller, W. O., Burks, M. T., Hagler, L. B., DeTeresa, S. J., & Witte, M. C., 2007. The MESSENGER Gamma-Ray and Neutron Spectrometer, *Space Science Reviews*, **131**, 339–391.

Hall, G. P., 2022. *X-ray Spectroscopy at Mercury with the Mercury Imaging X-ray Spectrometer*, Thesis, Department of Physics and Astronomy, University of Leicester.

Hall, G. P., Martindale, A., Paganini, A., Bridges, J. C., Lindsay, S. T., Tikkanen, T. V., & Bunce, E. J., 2025. DigiGREF: a digital analogue of the Mercury Imaging X-ray Spectrometer Ground-Reference Facility, *RAS Techniques and Instruments*, **4**.

Hawkins, S. E., Boldt, J. D., Darlington, E. H., Espiritu, R., Gold, R. E., Gotwols, B., Grey, M. P., Hash, C. D., Hayes, J. R., Jaskulek, S. E., Kardian, C. J., Keller, M. R., Malaret, E. R., Murchie, S. L., Murphy, P. K., Peacock, K., Prockter, L. M., Reiter, R. A., Robinson, M. S., Schaefer, E. D., Shelton, R. G., Sterner II, R. E., Taylor, H. W., Watters, T. R., & Williams, B. D., 2007. The Mercury dual imaging system on the MESSENGER spacecraft, *Space Science Reviews*, **131**, 247–338.

Hiesinger, H., Helbert, J., Alemanno, G., Bauch, K., D'Amore, M., Maturilli, A., Morlok, A., Reitze, M., Stangarone, C., Stojic, A., Varatharajan, I., Weber, I., & Team, M. C.-I., 2020. Studying the composition and mineralogy of the Hermean surface with the Mercury Radiometer and Thermal Infrared Spectrometer (MERTIS) for the BepiColombo mission: an update, *Space Science Reviews*, **216**, 1–37.

Ho, G. C., Starr, R. D., Gold, R. E., Krimigis, S. M., Slavin, J. A., Baker, D. N., Anderson, B. J., McNutt Jr, R. L., Nittler, L. R., & Solomon, S. C., 2011. Observations of suprathermal electrons in Mercury's magnetosphere during the three MESSENGER flybys, *Planetary and Space Science*, **59**(15), 2016–2025.

Hodoroaba, V.-D. & Rackwitz, V., 2014. Gaining improved chemical composition by exploitation of Compton-to-Rayleigh intensity ratio in XRF analysis, *Analytical chemistry*, **86**(14), 6858–6864.

Huovelin, J., Vainio, R., Kilpua, E., Lehtolainen, A., Korpela, S., Esko, E., Muinonen, K., Bunce, E., Martindale, A., & Grande, M., 2020. Solar intensity x-ray and particle spectrometer sixs: instrument design and first results, *Space Science Reviews*, **216**, 1–42.

Izenberg, N. R., Klima, R. L., Murchie, S. L., Blewett, D. T., Holsclaw, G. M., McClintock, W. E., Malaret, E., Mauceri, C., Vilas, F., Sprague, A. L., Helbert, J., Domingue, D. L., Head Iii, J. W., Goudge, T. A., Solomon, S. C., Hibbitts, C. A., & Darby Dyar, M., 2014. The low-iron, reduced surface of Mercury as seen in spectral reflectance by MESSENGER, *Icarus*, **228**, 364–374.

Jochum, K. P., Nohl, U., Herwig, K., Lammel, E., Stoll, B., & Hofmann, A. W., 2005. GeoReM: a new geochemical database for reference materials and isotopic standards, *Geostandards and Geoanalytical Research*, **29**(3), 333–338.

Kissel, L., 2000. RTAB: the Rayleigh scattering database, *Radiation Physics and Chemistry*, **59**(2), 185–200.

Klima, R. L., Denevi, B. W., Ernst, C. M., Murchie, S. L., & Peplowski, P. N., 2018. Global distribution and spectral properties of low-reflectance material on Mercury, *Geophysical Research Letters*, **45**(7), 2945–2953.

Labonville, F., Charbonneau, P., & Lemerle, A., 2019. A dynamo-based forecast of solar cycle 25, *Solar Physics*, **294**(6), 82.

Lark, L. H., Head, J. W., & Huber, C., 2023. Evidence for a carbon-rich mercury from the distribution of low-reflectance material (lrm) associated with large impact basins, *Earth and Planetary Science Letters*, **613**, 118192.

Lauf, T., 2011. *Analysis and operation of DePFET X-ray imaging detectors*, Thesis.

Machol, J., Viereck, R., Peck, C., & Mothersbaugh III, J., 2022. GOES X-ray Sensor (XRS) Operational Data, Report.

Majewski, P., Aschauer, F., Aschauer, S., Bähr, A., Bergbauer, B., Hilchenbach, M., Krumrey, M., Laubis, C., Lauf, T., & Lechner, P., 2014. Calibration measurements on the DEPFET Detectors for the MIXS instrument on BepiColombo, *Experimental Astronomy*, **37**(3), 525–538.

McClintock, W. E. & Lankton, M. R., 2007. The Mercury atmospheric and surface composition spectrometer for the MESSENGER mission, *Space Science Reviews*, **131**, 481–521.

Murchie, S. L., Klima, R. L., Denevi, B. W., Ernst, C. M., Keller, M. R., Domingue, D. L., Blewett, D. T., Chabot, N. L., Hash, C. D., & Malaret, E., 2015. Orbital multispectral mapping of mercury with the messenger mercury dual imaging system: Evidence for the origins of plains units and low-reflectance material, *Icarus*, **254**, 287–305.

Nittler, L. R., Starr, R. D., Weider, S. Z., McCoy, T. J., Boynton, W. V., Ebel, D. S., Ernst, C. M., Evans, L. G., Goldsten, J. O., & Hamara, D. K., 2011. The major-element composition of Mercury's surface from MESSENGER X-ray spectrometry, *Science*, **333**(6051), 1847–1850.

Nittler, L. R., Frank, E. A., Weider, S. Z., Crapster-Pregont, E., Vorburger, A., Starr, R. D., & Solomon, S. C., 2020. Global major-element maps of Mercury from four years of MESSENGER X-Ray Spectrometer observations, *Icarus*, **345**, 113716.

Nittler, L. R., Boujibar, A., Crapster-Pregont, E., Frank, E. A., McCoy, T. J., McCubbin, F. M., Starr, R. D., Vorburger, A., & Weider, S. Z., 2023. Chromium on Mercury: New results from the MESSENGER X-Ray Spectrometer and implications for the innermost planet's geochemical evolution, *Journal of Geophysical Research: Planets*, p. e2022JE007691.

Peplowski, P. N. & Stockstill-Cahill, K., 2019. Analytical identification and characterization of the major geochemical terranes of Mercury's northern hemisphere, *Journal of Geophysical Research: Planets*, **124**(9), 2414–2429.

Peplowski, P. N., Lawrence, D. J., Evans, L. G., Klima, R. L., Blewett, D. T., Goldsten, J. O., Murchie, S. L., McCoy, T. J., Nittler, L. R., & Solomon, S. C., 2015. Constraints on the abundance of carbon in near-surface materials on Mercury: Results from the MESSENGER Gamma-Ray Spectrometer, *Planetary and Space Science*, **108**, 98–107.

Peplowski, P. N., Klima, R. L., Lawrence, D. J., Ernst, C. M., Denevi, B. W., Frank, E. A., Goldsten, J. O., Murchie, S. L., Nittler, L. R., & Solomon, S. C., 2016. Remote sensing evidence for an ancient carbon-bearing crust on Mercury, *Nature Geoscience*, **9**(4), 273–276.

Perrett, G. M., Campbell, J. L., Gellert, R., King, P. L., Nield, E., O'Meara, J. M., & Pradler, I., 2016. Refinement of the Compton–Rayleigh scatter ratio method for use on the Mars Science Laboratory alpha particle X-ray spectrometer: II–Extraction of invisible element content, *Nuclear Instruments and Methods in Physics Research Section B: Beam Interactions with Materials and Atoms*, **368**, 129–137.

Phillips, K., 2004. The solar flare 3.8-10 keV X-ray spectrum, *The Astrophysical Journal*, **605**(2), 921.

Riner, M., Lucey, P., Desch, S., & McCubbin, F., 2009. Nature of opaque components on Mercury: Insights into a Mercurian magma ocean, *Geophysical Research Letters*, **36**(2).

Rivera-Valentin, E. G. & Barr, A. C., 2014. Impact-induced compositional variations on mercury, *Earth and Planetary Science Letters*, **391**, 234–242.

Robinson, M. S., Murchie, S. L., Blewett, D. T., Domingue, D. L., Hawkins III, S. E., Head, J. W., Holsclaw, G. M., McClintock, W. E., McCoy, T. J., McNutt Jr, R. L., Prockter, L. M., Solomon, S. C., & Watters, T. R., 2008. Reflectance and Color Variations on Mercury: Regolith Processes and Compositional Heterogeneity, *Science*, **321**(5885), 66–69.

Rothery, D. A., Massironi, M., Alemanno, G., Barraud, O., Besse, S., Bott, N., Brunetto, R., Bunce, E., Byrne, P., & Capaccioni, F., 2020. Rationale for BepiColombo studies of Mercury's surface and composition, *Space science reviews*, **216**(4), 1–46.

Schlemm, C. E., Starr, R. D., Ho, G. C., Bechtold, K. E., Hamilton, S. A., Boldt, J. D., Boynton, W. V., Bradley, W., Fraeman, M. E., Gold, R. E., Goldsten, J. O., Hayes, J. R., Jaskulek, S. E., Rossano, E., Rumpf, R. A., Schaefer, E. D., Strohbehn, K., Shelton, R. G., Thompson, R. E., Trombka, J. I., & Williams, B. D., 2007. The X-Ray Spectrometer on the MESSENGER spacecraft, *Space Science Reviews*, **131**, 393–415.

Schoonjans, T., Brunetti, A., Golosio, B., Del Rio, M. S., Solé, V. A., Ferrero, C., & Vincze, L., 2011. The xraylib library for X-ray–matter interactions. Recent developments, *Spectrochimica Acta Part B: Atomic Spectroscopy*, **66**(11-12), 776–784.

Solomon, S. C., Nittler, L. R., & Anderson, B. J., 2018. *Mercury: The view after MESSENGER*, vol. 21 of **Cambridge Planetary Science**, Cambridge University Press.

Sonke, A. & Robinson, M. S., 2024. Enhanced UV/visible reflectance of mercurian low reflectance material in MDIS-controlled Mariner 10 mosaics, in *Mercury 24*, Kyoto, Japan.

Starr, R. D., 2018. MESSENGER XRS Calibrated (CDR) Data Bundle.

Starr, R. D., Schlemm II, C. E., Ho, G. C., Nittler, L. R., Gold, R. E., & Solomon, S. C., 2016. Calibration of the MESSENGER X-ray spectrometer, *Planetary and Space Science*, **122**, 13–25.

Thomas, R. J., Rothery, D. A., Conway, S. J., & Anand, M., 2014. Hollows on Mercury: Materials and mechanisms involved in their formation, *Icarus*, **229**, 221–235.

Thomas, R. J., Hynek, B. M., Rothery, D. A., & Conway, S. J., 2016. Mercury's low-reflectance material: Constraints from hollows, *Icarus*, **277**, 455–465.

Trang, D., Lucey, P. G., & Izenberg, N. R., 2017. Radiative transfer modeling of messenger virs spectra: Detection and mapping of submicroscopic iron and carbon, *Icarus*, **293**, 206–217.

Vander Kaaden, K. E. & McCubbin, F. M., 2015. Exotic crust formation on Mercury: Consequences of a shallow, FeO-poor mantle, *Journal of Geophysical Research: Planets*, **120**(2), 195–209.

Weider, S. Z., Nittler, L. R., Starr, R. D., McCoy, T. J., & Solomon, S. C., 2014. Variations in the abundance of iron on Mercury's surface from MESSENGER X-Ray Spectrometer observations, *Icarus*, **235**, 170–186.

Weider, S. Z., Nittler, L. R., Murchie, S. L., Peplowski, P. N., McCoy, T. J., Kerber, L., Klimczak, C., Ernst, C. M., Goudge, T. A., & Starr, R. D., 2016. Evidence from MESSENGER for sulfur-and carbon-driven explosive volcanism on Mercury, *Geophysical Research Letters*, **43**(8), 3653–3661.

Xu, R., Xiao, Z., Wang, Y., & Cui, J., 2024. Less than one weight percent of graphite on the surface of Mercury, *Nature Astronomy*.